The Astrophysical Journal, 935:109 (16pp), 2022 August 20 https://doi.org/10.3847/1538-4357/ac8159

Reconstructing the Disrupted Dwarf Galaxy Gaia-Sausage/Enceladus Using Its Stars and Globular Clusters

Guilherme Limberg[1], Stefano O. Souza[1,2], Angeles Pérez-Villegas[3], Silvia Rossi[1], Hélio D. Perottoni[1], and Rafael M. Santucci[4,5]
[1] Universidade de São Paulo, Instituto de Astronomia, Geofísica e Ciências Atmosféricas, Departamento de Astronomia, SP 05508-090, São Paulo, Brazil
guilherme.limberg@usp.br
[2] Leibniz-Institut für Astrophysik Potsdam (AIP), An der Sternwarte 16, Potsdam, D-14482, Germany
[3] Instituto de Astronomía, Universidad Nacional Autónoma de México, Apartado Postal 106, C.P. 22800, Ensenada, B.C., Mexico
[4] Universidade Federal de Goiás, Instituto de Estudos Socioambientais, Planetário, Goiânia, GO 74055-140, Brazil
[5] Universidade Federal de Goiás, Campus Samambaia, Instituto de Física, Goiânia, GO 74001-970, Brazil
Received 2022 April 29; revised 2022 July 8; accepted 2022 July 13; published 2022 August 22

Abstract

We combine spectroscopic, photometric, and astrometric information from APOGEE data release 17 and Gaia early data release 3 to perform a self-consistent characterization of Gaia-Sausage/Enceladus (GSE), the remnant of the last major merger experienced by the Milky Way, considering stars and globular clusters (GCs) altogether. Our novel set of chemodynamical criteria to select genuine stars of GSE yields a metallicity distribution function with a median [Fe/H] of −1.22 and 0.23 dex dispersion. Stars from GSE present an excess of [Al/Fe] and [Mg/Mn] (also [Mg/Fe]) in comparison to surviving Milky Way dwarf satellites, which can be explained by differences in star formation efficiencies and timescales between these systems. However, stars from Sequoia, another proposed accreted halo substructure, essentially overlap the GSE footprint in all analyzed chemical-abundance spaces, but present lower metallicities. Among the probable GCs of GSE with APOGEE observations available, we find no evidence for atypical [Fe/H] spreads with the exception of ω Centauri (ωCen). Under the assumption that ωCen is a stripped nuclear star cluster, we estimate the stellar mass of its progenitor to be $M_\star \approx 1.3 \times 10^9 M_\odot$, well within literature expectations for GSE. This leads us to envision GSE as the best available candidate for the original host galaxy of ωCen. We also take advantage of Gaia's photometry and APOGEE metallicities as priors to determine fundamental parameters for eight high-probability (>70%) GC members of GSE via statistical isochrone fitting. Finally, the newly determined ages and APOGEE [Fe/H] values are utilized to model the age–metallicity relation of GSE.

Unified Astronomy Thesaurus concepts: Dwarf galaxies (416); Chemical abundances (224); Galaxy chemical evolution (580); Galactic archaeology (2178); Milky Way stellar halo (1060); Halo stars (699); Globular star clusters (656)

1. Introduction

Within the Λ cold dark matter (ΛCDM) paradigm (e.g., Planck Collaboration et al. 2020), galaxies and their dark matter halos grow in size through successive merging with other such systems (Press & Schechter 1974; White & Rees 1978; Faber & Gallagher 1979; Blumenthal et al. 1984; Kauffmann et al. 1993; Springel et al. 2006). The discovery of the Sagittarius (Sgr) dwarf spheroidal (dSph) galaxy, a satellite of the Milky Way undergoing tidal stripping (Ibata et al. 1994, 1995), provided a dramatic demonstration of this hierarchical assembly mechanism operating in the local universe.

Unlike the tidal tails (i.e., the "stream") of Sgr (Majewski et al. 2003; Belokurov et al. 2006; Law & Majewski 2010), the stellar debris of ancient (redshift $z \gtrsim 1$) accretion events are not expected to be recognized as strong spatial overdensities. As dwarf galaxies interact with the gravitational potential of the Milky Way, they are continuously disrupted until their original members are completely phase mixed into a smooth halo (Helmi & White 1999; McMillan & Binney 2008; Morinaga et al. 2019). Nevertheless, given the variety of star formation and chemical-enrichment histories likely experienced by these dwarf galaxies (Gallart et al. 2005; Tolstoy et al. 2009) as well as the different orbital properties of their associated mergers, the elemental abundances and dynamics of the stars born in these systems should make them discernible from in situ stellar populations (e.g., Freeman & Bland-Hawthorn 2002).

In a seminal work, Nissen & Schuster (2010) investigated nearby (mostly within $\lesssim$150 pc from the Sun) kinematically defined thick-disk and halo stars with overlapping metallicities ($-1.6 < [Fe/H] < -0.4$). Their key result was that the halo could be broadly divided into two stellar populations, the low- and high-α groups, in the [α[6]/Fe]–[Fe/H] diagram (Wallerstein 1962; Tinsley 1979). The chemical compositions of high-α stars were indistinguishable from the canonical thick-disk ones, reaching higher metallicities, and their velocity distribution appeared to constitute a dynamically *hotter* portion of it, being mostly on prograde orbits. On the contrary, low-α stars were more metal-poor and presented almost null net rotation with respect to the Galactic center, with many even showing retrograde motions.

The findings of Nissen & Schuster (2010) were remarkably corroborated by abundance information for much larger

[6] The specific α elements analyzed were Mg, Si, and Ti.

samples of halo stars (Hawkins et al. 2015; Hayes et al. 2018) derived from high-resolution ($\mathcal{R} \sim 22,500$) near-infrared (1.5–1.7 μm) spectra collected over the course of the Apache Point Observatory Galactic Evolution Experiment (APOGEE; Majewski et al. 2017) survey. Additionally, with the advent of photometric (in the optical) and astrometric data for millions of stars in the Milky Way, thanks to the Gaia mission (Gaia Collaboration et al. 2016), particularly its second data release (DR2; Gaia Collaboration et al. 2018a), a striking counterpart to the low–high-α dichotomy was found in the color–magnitude diagram (CMD) of high-velocity stars in the extended solar vicinity ($\sim$1.5 kpc). This halo CMD presented by Gaia Collaboration et al. (2018b, their Figure 21) revealed a bifurcation with two well-defined tracks, indicating the presence of distinct, a bluer (more metal-poor) and a redder (metal-rich), stellar populations in the local halo.

Almost at the same time, Koppelman et al. (2018; see also Gaia Collaboration et al. 2018c) made use of this exquisite Gaia DR2 data to analyze the kinematics of the halo near ($\sim$1.0 kpc) the Sun. These authors found a prominent, almost nonrotating, *blob* in the velocity distribution of halo stars. They also showed that this feature coincides with the bluer, metal-poor sequence in Gaia DR2's halo CMD. Furthermore, Belokurov et al. (2018) examined the global phase-space properties of the halo as a function of metallicity (see also Myeong et al. 2018b). It was clear that the stars within $-1.7 \lesssim [\mathrm{Fe/H}] < -1.0$ exhibited extreme radial anisotropy, with their orbits being highly eccentric, with almost no rotation around the Galactic center. This peculiar kinematic signature led Belokurov et al. (2018) to dub it the (Gaia-) "Sausage" due to its morphology in velocity space. The findings of both efforts were also impressively consistent with the properties of the prototypical low-α population as well as earlier studies (Chiba & Beers 2000; Carollo et al. 2007, 2010).

All the pieces of this puzzle were put together into a coherent picture in a work by Haywood et al. (2018) and complemented by Helmi et al. (2018). According to the latter's interpretation (based on preexisting simulations by Villalobos & Helmi 2008, 2009), stars on such acute radial orbits (i.e., the kinematic structure described by Koppelman et al. 2018 and Belokurov et al. 2018) correspond to the remnants of a single major merging (Conselice 2014) episode, with a mass ratio of 1/4 between the dwarf galaxy and the Milky Way at the epoch of its occurrence approximately 10 Gyr ago (redshift $z \sim 1.8$). Moreover, the collision with this relatively massive (stellar mass $M_\star \sim 10^{8.5}$–$10^{9.5} M_\odot$) galaxy, which was named "Gaia-Enceladus," probably carried enough kinetic energy to dynamically heat a primordial disk, leading to the formation of the thick disk along with its hotter component (the high α—redder track, constituting an in situ halo; Di Matteo et al. 2019), in line with theoretical predictions (Zolotov et al. 2009; Purcell et al. 2010; Qu et al. 2011; Tissera et al. 2013).

The propositions of Haywood et al. (2018) and Helmi et al. (2018) have, so far, been substantiated by numerous other studies with a myriad of approaches. Those include the inspection of Milky Way–mass halos with Gaia-Sausage/Enceladus (GSE) analogs in cosmological hydrodynamical simulations (Bignone et al. 2019; Fattahi et al. 2019; Elias et al. 2020; Grand et al. 2020), the detailed star formation history of (bluer–redder sequence) halo stars (Gallart et al. 2019), chemical-evolution modeling (Vincenzo et al. 2019), the phase-space (Iorio & Belokurov 2019; Lancaster et al. 2019; Simion et al. 2019; Iorio & Belokurov 2021) and chemodynamical (Deason et al. 2018; Naidu et al. 2020) properties of distant halo tracers, and the precise ages of thick-disk and halo stars from asteroseismology (Montalbán et al. 2021).

In the context of this emerging Galactic storyline, where the infall of GSE was largely responsible for shaping the present-day global structure of the Milky Way, it would also be expected that such a massive galaxy should host its own system of globular clusters (GCs). The first attempt at directly attributing Milky Way GCs to GSE was made by Myeong et al. (2018c) based on their agglomeration in integrals-of-motion space. A similar investigation was conducted by Massari et al. (2019), but with a much larger sample of GCs with full six-dimensional phase-space information from Gaia DR2 (Gaia Collaboration et al. 2018d; Vasiliev 2019a). The main conclusion reached by both studies was that GCs dynamically vetted to be associated with GSE follow an age–metallicity relation (AMR) compatible with a dwarf-galaxy origin (e.g., Leaman et al. 2013). Massari et al. (2019; also Pfeffer et al. 2021) further suggested that NGC 5139/ω Centauri (ωCen) could be the surviving nuclear star cluster (NSC) of GSE.

It is clear that, to comprehend the true impact of the GSE merger in the evolution of the Milky Way and gain insights about how GSE-mass galaxies looked like at high redshift, we need to characterize both its stellar and GC populations and put them in context with observations of the local universe. Fortunately, the combination between APOGEE's spectroscopic and Gaia's photometric and astrometric information for field and GC stars alike consists of a suitable sample for this task. Therefore, the objective of the present contribution is to construct a complete view of GSE, including its probable stars and GCs, in the most homogeneous, self-consistent manner currently possible. In the process, we build upon the literature, which is pulverized across many works employing different data sets, to test whether or not their interpretations remain valid when considering field stars and GCs altogether.

This paper is organized as follows. Section 2 describes the data sets utilized throughout this work, namely APOGEE data release 17 (DR17; Abdurro'uf et al. 2022) and Gaia early data release 3 (EDR3; Gaia Collaboration et al. 2021). All analyses regarding the stellar population of GSE are described in Section 3, e.g., sample selection, abundance patterns, and comparisons with nearby galaxies. In Section 4, the properties of GCs associated with GSE are explored, including NSC candidates, the determination of ages with APOGEE metallicity input, and the derivation of their final AMR. Finally, a summary of our conclusions is provided in Section 5.

2. Data

2.1. APOGEE DR17+Gaia EDR3

Throughout this work, we analyze publicly available data from APOGEE DR17. The reduction pipeline, including line-of-sight velocity (v_{los}) determination, was described by Nidever et al. (2015). Effective temperature (T_{eff}), surface gravity ($\log g$), and abundance values were obtained via the APOGEE Stellar Parameter and Chemical Abundance Pipeline (ASPCAP; García Pérez et al. 2016). See Jönsson et al. (2020) for the previous application of these tools. To ensure the accuracy of the information at hand, we performed a series of standard quality-control cuts. Only the stars with reasonably

high signal-to-noise ratios ($S/N > 50$ pixel^{-1}) and reliable spectral fittings (STARFLAG = 0 and ASPCAPFLAG = 0) were considered, avoiding suspect determinations of the aforementioned quantities. We also limited our sample to giant stars by requiring $3500\,K < T_{\rm eff} < 6000\,K$ and $\log g < 3.5$. In practice, these cuts are similar to those preferred in recent efforts that used APOGEE DR17 data (Hasselquist et al. 2021; Queiroz et al. 2021; Horta et al. 2022). Moreover, we separate field stars from GC ones according to the catalog of Vasiliev & Baumgardt (2021; see our Section 2.2), which provides the individual membership probabilities based on astrometric quantities from Gaia EDR3. We also discard all field stars with problematic (i.e., flagged) estimates of [Fe/H], [Mg/Fe], [Al/Fe], and [Mn/Fe].

This sample of field stars from APOGEE DR17 was cross-matched (1″.5 search radius) with the Gaia EDR3 complete catalog to obtain parallaxes and absolute proper motions (PMs). In order to guarantee a high quality of the astrometric solutions, we only retained the stars with renormalized unit weight errors within the recommended range (RUWE $\leqslant 1.4$; Lindegren et al. 2021a), following the standard practices for usage of Gaia EDR3 data (e.g., Fabricius et al. 2021). Moreover, we require parallax_over_error > 2 in order to remove stars associated with dwarf satellite galaxies (including the Sgr stream) that were also targeted during the course of APOGEE (Beaton et al. 2021; Santana et al. 2021; Abdurro'uf et al. 2022).

For all field stars, we adopted spectro-photoastrometric heliocentric distances ($d_\odot$) estimated with the Bayesian isochrone-fitting code StarHorse[7] (Santiago et al. 2016; Queiroz et al. 2018), which already accounts for parallax biases (Lindegren et al. 2021b). StarHorse combines high-resolution spectroscopic information from APOGEE, broadband photometry from various sources (see Anders et al. 2019), and Gaia EDR3 parallaxes to obtain $d_\odot$ under the prior assumption of a three-dimensional model of the Galaxy (Queiroz et al. 2020). Lastly, we restricted our sample to stars with moderate (<20%) fractional uncertainties, assuming Gaussian distributions, of their nominal $d_\odot$ values.

2.2. Globular Cluster Catalog

As already mentioned, we identified the stars confidently attributed to GCs within the recent catalog of Vasiliev & Baumgardt (2021). These authors calculated the probabilities of individual stars being members of known Galactic GCs with a mixture model technique that took into account parallaxes and PMs made available by Gaia EDR3. In this work, whenever a star in assumed to belong to a GC, it means that its membership probability is >99%. Genuine GC stars were, then, matched (1″.5 radius) with APOGEE DR17.

We further utilize the summary of Galactic GC properties provided by Vasiliev & Baumgardt (2021). This compilation includes an expanded list of (170) GCs with mean PMs estimated via the aforementioned mixture modeling method, $d_\odot$ derived by Baumgardt & Vasiliev (2021) from a combination between Gaia EDR3 and literature data, and $v_{\rm los}$ measured from ground-based instruments (Baumgardt et al. 2019).

[7] https://www.sdss.org/dr16/data_access/value-added-catalogs/?vac_id=apogee-dr17-starhorse-distances,-extinctions,-and-stellar-parameters

2.3. Kinematics and Dynamics

Positions on the sky, PMs, $v_{\rm los}$, and $d_\odot$ for field stars and GCs alike were converted into all phase-space quantities of interest. For this purpose, the Milky Way fundamental parameters adopted are those from McMillan (2017). Specifically, the distance from the Sun to the Galactic center is 8.2 kpc (Bland-Hawthorn & Gerhard 2016; compatible with Gravity Collaboration et al. 2019), the velocity of the local standard of rest (LSR) is $v_{\rm LSR} = 232.8\,{\rm km\,s^{-1}}$, and the peculiar motion of the Sun with respect to the LSR is $(U, V, W)_\odot = (11.10, 12.24, 7.25)\,{\rm km\,s^{-1}}$ (Schönrich et al. 2010).

Under identical assumptions, we integrate the orbits of both field stars and GCs for 10 Gyr forward in the axisymmetric Galactic potential model of McMillan (2017), in line with previous efforts (Massari et al. 2019; Souza et al. 2021), which includes a flattened bulge, thin and thick stellar disks, gaseous disks, and a spherical dark matter halo. We account for (Gaussian) errors in the above-mentioned input quantities by performing 100 Monte Carlo (MC) realizations of each star/GC's orbit. The final adopted kinematic/dynamical parameters are the medians of the resulting distributions while the 16th and 84th percentiles are taken as the associated uncertainties. For this task, we used the AGAMA (Vasiliev 2019b) library, which also computes orbital energies (E) and actions: J_R (radial component), J_ϕ (azimuthal), and J_z (vertical) in a cylindrical coordinate system. See Trick et al. (2019) for a practical interpretation of actions. We recall that the azimuthal action is equivalent to the z-component of angular momentum (L_z). Hence, we prefer the L_z nomenclature whenever this quantity is mentioned. In this right-handed frame, the negative values of L_z signify that the trajectory of a given object is prograde, with rotational motion in the same orientation as the Galactic disk.

3. Stellar Population of GSE

3.1. Selection of GSE Stars

In order for us to achieve a realistic characterization of the stellar population of GSE, the first step is to delineate our selection criteria. Past works proposed a multitude of methods for isolating the genuine members of this substructure (Koppelman et al. 2019a; Mackereth et al. 2019; Matsuno et al. 2019; Myeong et al. 2019; Feuillet et al. 2020; Naidu et al. 2020; Lane et al. 2022), including applications of sophisticated unsupervised learning–clustering algorithms (Borsato et al. 2020; Necib et al. 2020; Yuan et al. 2020; Limberg et al. 2021a; Gudin et al. 2021; Shank et al. 2022). Hence, we build upon these previous experiences to construct a suitable sample of GSE stars given our stated goals.

Among the above-listed studies, Feuillet et al. (2020) defined a box in $(L_z, \sqrt{J_R})$ space specifically designed to yield a minimal contamination from in situ stars, mostly from the thick disk, in GSE samples. These authors demonstrated that stars within $-500 \leqslant L_z \leqslant +500\ {\rm kpc\,km\,s^{-1}}$ and $30 \leqslant \sqrt{J_R} \leqslant 50\ ({\rm kpc\,km\,s^{-1}})^{1/2}$ constitute a narrow, single-peaked metallicity distribution function (MDF), akin to present-day Milky Way satellites (Kirby et al. 2011), which was interpreted as compelling evidence for a shared origin (within the progenitor of GSE) for such objects. Despite the Galactic potential model (MWpotential2014; Bovy 2015) employed by Feuillet et al. (2020) being different from the one adopted in our calculations, several studies have already shown that their strategy for isolating GSE stars can be satisfactorily

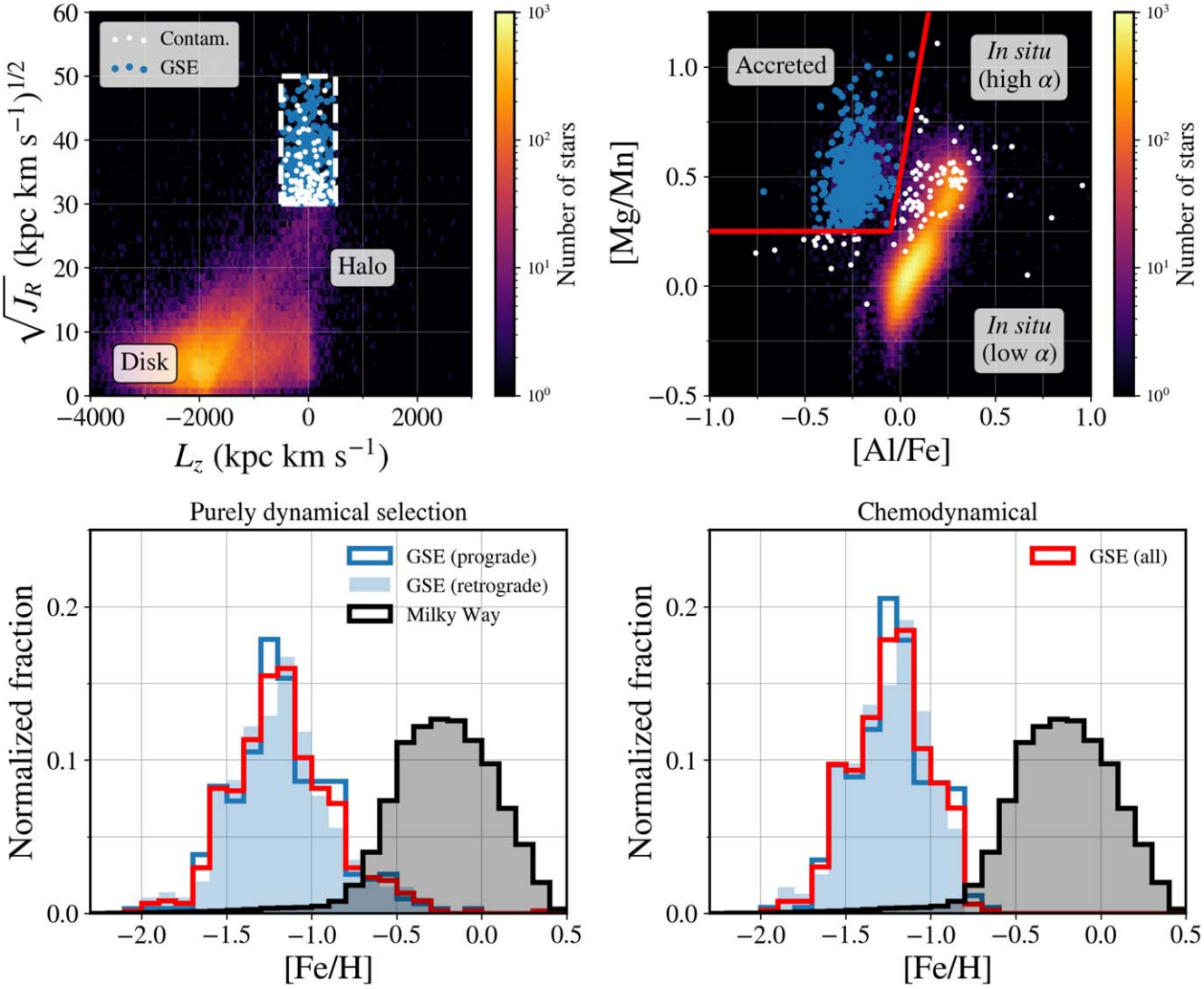

Figure 1. Top left: (L_z, $\sqrt{J_R}$). The dashed box delineates the purely dynamical criteria for vetting GSE stars. Blue dots belong to the clean GSE sample while white ones are considered contaminants (Section 3.1) Top right: [Mg/Mn]–[Al/Fe]. Red lines define the locus of accreted stars. Bottom left: MDFs of both GSE (blue and red) and the Milky Way–full sample (black). For GSE, the [Fe/H] distributions are divided into prograde (empty histogram) and retrograde (filled) portions (Section 3.2). The red histogram shows the combined MDF (prograde and retrograde stars altogether). Bottom right: same as previous panel, but only accounting for stars within the final chemodynamical selection (only blue dots; Equation (1)) for GSE.

implemented for the latter (Matsuno et al. 2021; Perottoni et al. 2021; Buder et al. 2022). Therefore, we choose this selection (top left panel of Figure 1) as a starting point, but conducted our own critical assessment of its quality regardless.

We evaluate the purity of the resulting sample of GSE candidates constructed with the Feuillet et al. (2020) pair of criteria by estimating the fraction of stars with disk-like chemistry (e.g., Hayden et al. 2015) in it, which we refer to as "contamination." For this exercise, it is convenient that past works have explored which combinations of elemental abundances, among those available from APOGEE data, are best suited to differentiate between accreted and in situ populations, notably Hawkins et al. (2015) and, recently, Das et al. (2020). These authors found, from an empirical standpoint, that the space defined by [Al/Fe]–[Mg/Mn] is the most efficient for this separation. The top right panel of Figure 1 shows our application of this abundance plane, where the boundary lines between components (labels inside the plot) are similar to Horta et al. (2021; see also Queiroz et al. 2021 and Naidu et al. 2022).

From Figure 1, it is clear that the majority of potential GSE members within the described selection box (dashed lines) truly occupies the locus of ancient ($\gtrsim$10 Gyr; see Horta et al. 2021) accreted stars in the [Mg/Mn]–[Al/Fe] plane. However, there persists a significant amount of stars with chemical compositions similar to (mostly high-α) disk ones. This contamination (white dots) is at the level of $\sim$18%. Stars from other merging events might also be present, but their contribution should be negligible taking into account that the GSE system is expected to be much more massive than any other accreted dwarf galaxy identified so far (Helmi 2020; see also Buder et al. 2022).

We consolidated our clean GSE sample by discarding the stars with chemical abundances compatible with the in situ regions of the [Al/Fe]–[Mg/Mn] space. Therefore, throughout

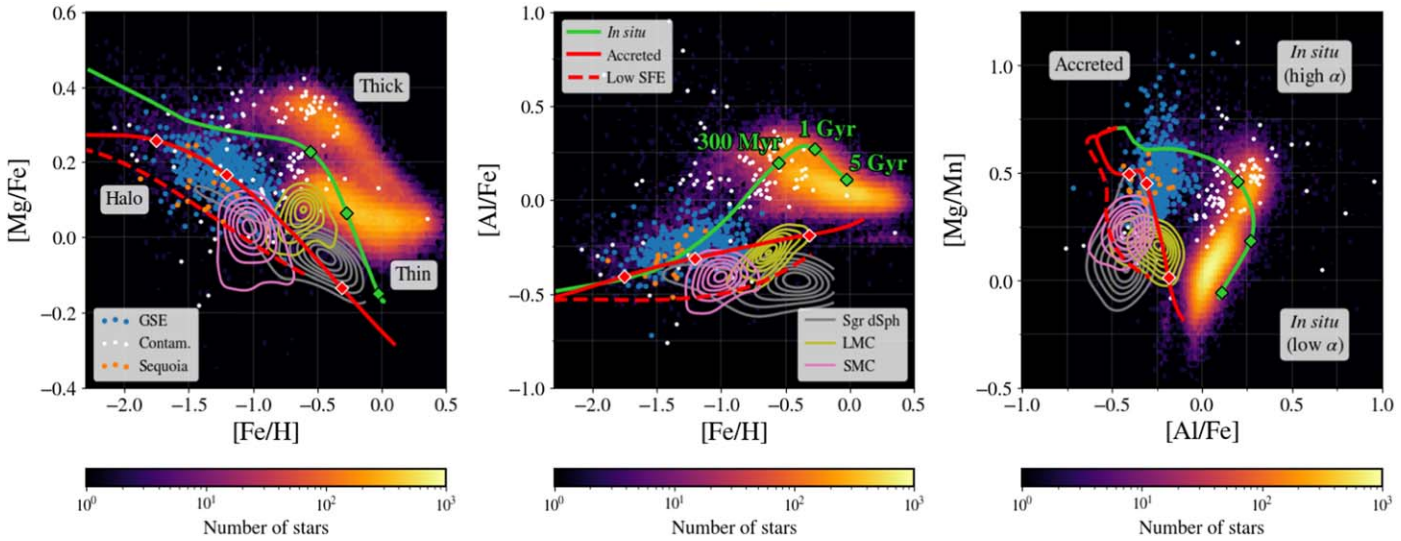

Figure 2. Left: [Mg/Fe]–[Fe/H]. Middle: [Al/Fe]–[Fe/H]. Right: [Mg/Mn]–[Al/Fe]. Stars of GSE and Sequoia (Section 3.4) are displayed as blue and orange dots, respectively. As in Figure 1, white symbols are considered contaminants (Section 3.1). Abundance patterns of dwarf satellite galaxies are shown as colored contours; Sgr dSph (gray), LMC (yellow), and SMC (pink). Chemical-evolution models representative of in situ and accreted stellar populations are overlaid as green and red lines, respectively. The dashed line is analogous to the *accreted* model, but with a reduced (by 80%) SFE (see text). The associated green–red symbols on top of these lines highlight certain epochs (0.3, 1.0, and 5.0 Gyr) after the beginning of star formation.

the remainder of this paper, a star is considered a confident member of GSE if it respects the following conditions:

$$\text{GSE} = \begin{cases} -500 \leqslant L_z \leqslant +500 \text{ kpc km s}^{-1} \\ 30 \leqslant \sqrt{J_R} \leqslant 50 \text{ (kpc km s}^{-1})^{1/2} \\ \text{[Mg/Mn]} > +0.25 \\ \text{[Mg/Mn]} > 5 \times \text{[Al/Fe]} + 0.5, \end{cases} \quad (1)$$

which can be readily reproduced.

3.2. MDF(s) of GSE

With the list of (∼500) confident members of GSE at hand, we begin our characterization of this population. In the bottom panels of Figure 1, we compare the MDFs derived via the purely dynamical approach (Feuillet et al. 2020; left panel) with the chemodynamical one (right) adopted in this work. From an immediate visual inspection, we notice that the global MDF (red histogram) of the former is broader (larger dispersion) in comparison to the latter, showing an excess of stars toward the metal-rich ([Fe/H] $\gtrsim -0.7$) regime. Although this result might be expected, because we removed the stars with disk-like chemistry from our clean GSE sample, we never make an explicit cut in [Fe/H]. Therefore, it is reassuring that we can confirm this behavior from the data. Quantitatively, we found a median [Fe/H] of −1.20 dex and a median absolute deviation (MAD) of 0.27 dex when considering all stars within the box in (L_z, $\sqrt{J_R}$). Upon incorporating the chemical portion of our selection, the median [Fe/H] of our final GSE members is −1.22 dex with a MAD of 0.23 dex.

We further test the self-consistency of the resulting MDFs by dividing them into prograde ($L_z < 0$) and retrograde ($L_z > 0$) portions and performing a simple comparison (blue histograms in Figure 1). In each case, both merely dynamical and chemodynamical GSE selections, we apply a standard Kolmogorov–Smirnov test between prograde and retrograde MDFs. We concluded that we cannot discard the null hypothesis that the MDFs were drawn from the same parent distributions (p-value >0.93 for the purely dynamical case and >0.85 for the chemodynamical one). This so-called "homogeneity" across these MDFs was used as the main argument by Feuillet et al. (2020) when asserting that their criteria yielded the least contaminated GSE sample. Therefore, it is crucial that our consolidated sample retains this property.

At last, we can compare our findings with past metallicity determinations for the GSE stellar population. Helmi et al. (2018) originally noticed a peak around [Fe/H] ≈ −1.6 from their study with APOGEE DR14 (Abolfathi et al. 2018) abundances. However, the literature quickly converged to higher values. This is likely due to the presence of (very) metal-poor stars not associated with GSE, but rather retrograde debris (Myeong et al. 2018a, 2018d; Koppelman et al. 2019a; Yuan et al. 2020; Limberg et al. 2021a; Shank et al. 2022) of other merging events of smaller scales, within the sample of Helmi et al. (2018). For instance, Myeong et al. (2019) analyzed the same APOGEE DR14 data and argued that the peak of GSE's MDF was closer to [Fe/H] = −1.3 (see also Matsuno et al. 2019; and Amarante et al. 2020), slightly more metal-poor than this work's value, given a much stricter selection criteria. Naidu et al. (2020) derived an even higher value of −1.15 dex (also An & Beers 2021) for the median [Fe/H] of GSE stars with data from the Hectochelle in the Halo at High Resolution (H3; Conroy et al. 2019) survey. The median [Fe/H] value of −1.22 dex presented in this work (chemodynamical approach) is broadly consistent with these previous results, but inclined toward a more metal-rich GSE.

3.3. Abundance Patterns

With APOGEE spectroscopic data, we extend the characterization of GSE in terms of various elements. Figure 2 shows several abundance planes previously empirically recognized to be most appropriate for segregating the halo stars from thin–thick disk ones (Hawkins et al. 2015; Das et al. 2020), namely [Mg/Fe]–[Fe/H] (left), [Al/Fe]–[Fe/H] (middle), and [Mg/Mn]–[Al/Fe] (right). Indeed, in all of these diagrams, the members of GSE are clearly discernible from the stars with disk-like compositions (yellowish–lighter regions of the plots).

Figure 2 further displays stars on high-energy retrograde orbits, also proposed to be of accreted origin, which are dubbed "Sequoia" (Myeong et al. 2019, but see Section 3.4 for the complete discussion), and the footprint of surviving satellite galaxies with observations conducted during the course of APOGEE, namely Sgr dSph (gray contours) and Large Magellanic Cloud–Small Magellanic Cloud (LMC–SMC; yellow–pink). Genuine stars from these galaxies were selected as in Hayes et al. (2020, for Sgr dSph) and Nidever et al. (2020, SMC/LMC), but discarding those with RUWE $\leqslant 1.4$ for consistency with the Galactic field-star sample (as in Section 2.1). Despite some overlap, these dwarf galaxies are distinguishable from both the GSE and the Milky Way.

Figure 2 also includes one-zone chemical-evolution models representative of in situ (green line) and accreted (red) stellar populations, illustrating a theoretical counterpart to the above-mentioned idea of segregating these groups within the presented chemical-abundance planes. The dashed line is a model similar to the *accreted* one, but with a star formation efficiency (SFE) reduced by 80%. These chemical-evolution trajectories were computed with the publicly available flexCE[8] code (Andrews et al. 2017) under the instantaneous mixing approximation. For the sake of consistency, the input parameters (initial gas mass, mass-loading factor, SFE) and basic assumptions (initial mass function and nucleosynthesis yields) are the same as those in Horta et al. (2021; see details in Appendix A). In this work, the models provide intuition regarding the different timescales for metal enrichment between massive (Milky Way) and dwarf (GSE and surviving satellites) galaxies. Overall, the *accreted* model roughly follows the regions occupied by GSE and the other dwarf galaxies. On the other hand, the "in situ" one is enriched much faster, as expected for a system with larger amounts of (cold and dense) gas available to form stars (e.g., Kennicutt 1998) and massive enough to retain the material expelled during energetic supernova explosions (Veilleux et al. 2005), and follows the regions predominantly inhabited by the Galactic disk(s).

In the [Mg/Fe]–[Fe/H] diagram (left panel of Figure 2), the GSE population constitutes a declining sequence within $-1.5 \lesssim$ [Fe/H] < -0.7, but with lower values of [Mg/Fe] for this metallicity range in comparison to the bulk of the Milky Way. Such behavior is equivalent to the low-α stars of Nissen & Schuster (2010) and is qualitatively reproduced by the models. Unlike the surviving dwarf galaxies, the distribution of [Mg/Fe] for GSE shows neither increase nor flattening toward the metal-rich regime, indicative of a star formation history with a single burst that was probably halted by the interaction with the Milky Way.

Within the same metallicity interval, we highlight that GSE has a higher (by ∼0.15–0.20 dex) typical [Al/Fe] in comparison to the other dwarf galaxies. According to the models overlaid in the middle panel of Figure 2, such a feature can be explained by a lower SFE for the surviving Milky Way satellites at early times, prior to the merger of GSE. Finally, the average [Mg/Mn] of GSE is also higher (∼0.25–0.35 dex) than that of Sgr dSph, LMC, and SMC (right panel of Figure 2). Although our final GSE selection (Equation (1)) includes an explicit cut in [Mg/Mn] > 0.25, this property exists for the purely dynamical approach as well (top row of Figure 1). The high values of both $\langle$[Al/Fe]$\rangle$ and $\langle$[Mg/Mn]$\rangle$ (also $\langle$[Mg/Fe]$\rangle$) at the same [Fe/H] reveal that the chemical enrichment of GSE had a contribution of core-collapse supernovae greater than the type Ia kind[9] in comparison to the other dwarfs (see Hasselquist et al. 2021), as expected for a galaxy with a star formation that was quickly interrupted. On the contrary, the extended chemical-enrichment histories of the surviving satellites allow them to reach lower values of [Mg/Mn] ([Mg/Fe]).

3.4. GSE and Sequoia

The proposition that another relevant merging event, the Sequoia, contributed to the assembly of the local halo culminated in the work of Myeong et al. (2019). Member stars of this substructure are characterized by their high orbital energies and peculiar retrograde motions (Koppelman et al. 2019a; Borsato et al. 2020; Yuan et al. 2020; Limberg et al. 2021a). However, the true nature of Sequoia is still not a consensus. With the aid of *N*-body simulations, Koppelman et al. (2020) demonstrated that the accretion of a GSE-mass disk-dominated galaxy could explain the retrograde tail in the velocity distribution of nearby (<1 kpc) halo stars without the necessity of invoking any additional mergers (see also Helmi et al. 2018).

Upon analyzing a much larger sample (from the H3 survey) of stars on high-energy retrograde orbits than previously considered, Naidu et al. (2020) concluded that the metal-rich ([Fe/H] $\gtrsim -1.4$) portion of this population's MDF, which they refer to as "Arjuna," closely followed the [Fe/H] distribution of GSE. For simplicity, we adopt the more usual *Sequoia* nomenclature to describe this population. In a subsequent paper, Naidu et al. (2021) took this tentative connection, with these stars constituting a retrograde tail of GSE, as a constraint to reconstruct the GSE merger through a pure *N*-body approach. These authors further combined their models with abundance data to predict a weak metallicity gradient, comparable to some dSph satellites (Kirby et al. 2011), for GSE. Indeed, Horta et al. (2022) explored numerical simulations of GSE-like mergers that account for star formation in both satellites and massive companions. They confirmed that GSE-mass galaxies naturally develop radial [Fe/H] gradients prior to their accretion, resulting in the complex present-day chemodynamical signatures in the halos of their hosts that include retrograde metal-poor features consistent with Sequoia-like properties.

Motivated by this emerging scenario, accurately determining the MDF of the high-energy retrograde halo population is of enormous importance. We vetted Sequoia candidates with the criteria recommended by Myeong et al. (2019), which uses the complete action vector; $L_z/J_{\rm total} > +0.5$ and $(J_z - J_R)/J_{\rm total} < +0.1$, where $J_{\rm total} = J_R + |L_z| + J_z$. We further constrain our Sequoia sample to high orbital energy values; $E > -1.4 \times 10^5$ km^2 s^{-2}, avoiding contamination from other retrograde substructures (we refer the reader to Koppelman et al. 2019a; Naidu et al. 2020; and Limberg et al. 2021a for detailed discussions). For consistency, we only consider a star to be a genuine member of Sequoia if it inhabits the accreted region of the [Mg/Mn]–[Al/Fe] diagram (right panel of Figure 2).

[8] https://github.com/bretthandrews/flexCE

[9] See, e.g., Nomoto et al. (2013) for discussions regarding the nucleosynthesis yields in both production sites.

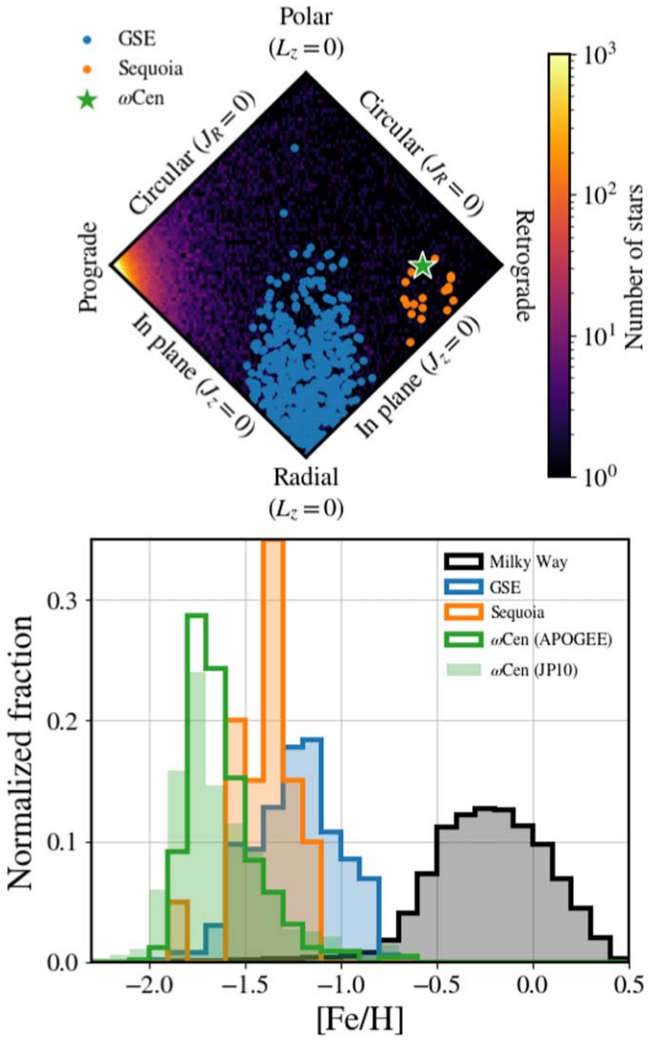

Figure 3. Top: projected action space. The horizontal axis displays $L_z/J_{\rm total} \in [-1, +1]$, where $J_{\rm total} = J_R + |L_z| + J_z$ (see text). Positive and negative values of this quantity indicate retrograde and prograde motions, respectively. The vertical axis shows $(J_z - J_R)/J_{\rm total} \in [-1, +1]$. One can notice the prograde stars galore toward the left corner of the plot due to the presence of the Galactic disk(s). Blue and orange dots are stars from GSE and Sequoia, respectively. The green star symbol marks the position of ωCen. Bottom: normalized MDFs of GSE (blue), Milky Way–full sample (black), Sequoia (orange), and ωCen (green). For ωCen, we display [Fe/H] distributions derived from both infrared (APOGEE DR17; empty histogram) and optical (filled; Johnson & Pilachowski 2010) spectra.

The distribution of the resulting sample (20 stars) within the projected action space is shown in the top row of Figure 3.

The MDF for Sequoia candidates is presented in the bottom row of Figure 3 (orange histogram). From an immediate visual inspection of this plot, the metal-rich side of this population's MDF does not track GSE's as closely as that in Naidu et al. (2020, 2021). Overall, the identified peak, at [Fe/H] ≈ -1.35, in the MDF of these high-energy retrograde stars is more metal-poor, by $\approx$0.15 dex, than the value reported by these authors.

Under the assumption that Sequoia is associated with GSE, we revisit the steps of Naidu et al. (2021) to estimate the metallicity gradient of the original galaxy. We substitute their [Fe/H] values with those found in this work and consider the same structural parameters for GSE. The final [Fe/H] gradient calculated is $-0.04^{+0.02}_{-0.03}$ dex kpc^{-1}, where the upper and lower limits represent bootstrapped (10^4 times) 95% confidence intervals. This value is equivalent to the one recently found by Horta et al. (2022). This gradient is also compatible with the LMC (Cioni 2009) as well as the local (redshift $z < 0.03$) star-forming galaxies of similar mass (Ho et al. 2015), but is larger than the one found by Naidu et al. (2021). Despite the small number of stars considered, this exercise highlights how sensitive the measured gradient is to the MDF of this high-energy retrograde population.

With the sample of Sequoia candidates at hand, we also compare this population with GSE in terms of other elemental-abundance ratios. We advert that these high-energy retrograde stars essentially overlap with GSE in all panels of Figure 2 (also Horta et al. 2022). Recently, Matsuno et al. (2022) argued that sufficiently high precision ($\lesssim$0.07 dex) in abundance estimates should allow us to distinguish between Sequoia and GSE. Despite the nominal uncertainties for [Mg/Fe] in our clean APOGEE DR17 data being small enough (<0.05 dex) for the majority ($\sim$97%) of all metal-poor ([Fe/H] < -1.0) stars, we did not find differences nearly as clear as reported by these authors (their Figure 5). Nevertheless, we note that this result might be related to the [Fe/H] range probed by the APOGEE data analyzed being tailored toward higher metallicities, i.e., more akin to Naidu et al's (2020) Arjuna, in comparison to the prototypical Sequoia (Myeong et al. 2019; also Matsuno et al. 2019; Monty et al. 2020; and Aguado et al. 2021).

3.5. The Mass of GSE

The first estimate of the $M_\star$ of GSE within the paradigm that this population represents the debris of a single accreted dwarf galaxy was presented by Helmi et al. (2018). Integrating the star formation rate over the time from the chemical-evolution model of Fernández-Alvar et al. (2018), these authors found $M_\star \sim 6 \times 10^8$ $M_\odot$, slightly more massive than the SMC ($M_\star = 4.6 \times 10^8$ $M_\odot$[10]). However, with a similar approach, Vincenzo et al. (2019) found a much higher value of $\approx 5 \times 10^9$ $M_\odot$ for the $M_\star$ of GSE, which would make the progenitor system of GSE even more massive than the LMC ($M_\star = 1.5 \times 10^9$ $M_\odot$). A higher $M_\star$ for GSE is also supported by the study of Feuillet et al. (2020), who found $\sim 2.5 \times 10^9 M_\odot$ based on a redshift-dependent stellar mass–metallicity relation (MZR; Ma et al. 2016). On the other hand, Forbes (2020) utilized a scaling relation between the number of GCs in a galaxy and its mass to determine the $M_\star$ of GSE. These authors reached $M_\star \approx 8 \times 10^8 M_\odot$, similar to the original calculation of Helmi et al. (2018). Lastly, Kruijssen et al. (2020) obtained $M_\star \sim 3 \times 10^8 M_\odot$ by comparing the AMR established by GCs of GSE with cosmological simulations (Pfeffer et al. 2018; Kruijssen et al. 2019a).

A rough average between the above-listed estimates for the $M_\star$ of GSE is $\sim 10^9$ $M_\odot$, which is assumed as representative for us to compare this substructure with Local Group galaxies. We also adopt a 1 dex range in $\log(M_\star/M_\odot)$ to establish upper and lower limits for the $M_\star$ of GSE. This range ($8.5 \leqslant \log(M_\star/M_\odot) \leqslant 9.5$; Figure 4) covers all literature values with the exception of the most extreme ones (Vincenzo et al. 2019; Kruijssen et al. 2020). The 1 dex confidence interval in $\log(M_\star/M_\odot)$ is also arbitrarily applied for Sgr dSph, LMC, and SMC in Figure 4 as the catalog utilized as a reference (McConnachie 2012) does not report appropriate uncertainties for this parameter. The mean [Fe/H] data for these surviving satellite galaxies, according to

[10] The $M_\star$ values for SMC, LMC, Sgr dSph are all taken from the McConnachie (2012) catalog.

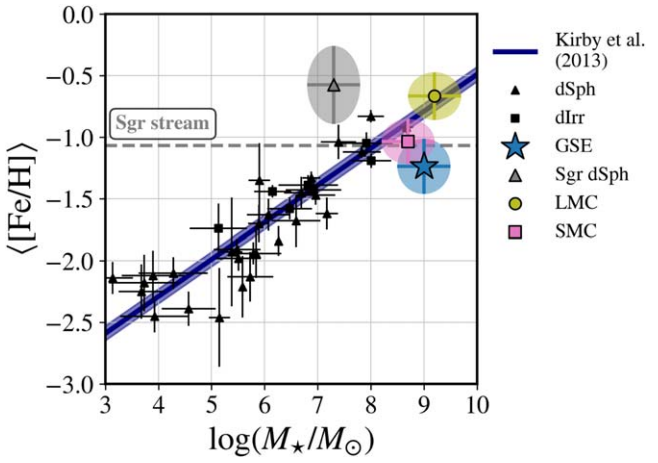

Figure 4. ⟨[Fe/H]⟩ vs. $M_\star$ for galaxies in the Local Group. Triangles and squares represent the sample of dSph and dwarf irregular (dIrr) galaxies, respectively, of Kirby et al. (2013). The dark blue line marks the MZR derived by these authors for the same galaxies. Colored symbols are reserved for the Milky Way satellites with abundance information in APOGEE DR17—Sgr dSph (gray), LMC (yellow dot), and SMC (pink, also a dIrr)—as well as for GSE (blue). The $M_\star$ estimates for these galaxies are taken from the catalog of McConnachie (2012). The overlapped ellipses, following the same color scheme, display 1 dex interval in $\log(M_\star/M_\odot)$ and the standard deviation of these galaxies' MDFs (see text). We also include a dashed gray line that illustrates the ⟨[Fe/H]⟩ of the Sgr stream.

APOGEE DR17, are −0.58, −0.67, and −1.04 dex, respectively, with standard deviations of 0.32, 0.19, and 0.18 dex (vertical axis of the ellipses shown in Figure 4). For GSE, $\langle[Fe/H]\rangle = -1.24$ with a dispersion of 0.23 dex.

We immediately notice that the high metallicity of Sgr dSph, combined with its low $M_\star$, is, at first glance, violating the MZR of Kirby et al. (2013). However, we recall that this galaxy is well known to be experiencing severe tidal stripping (Majewski et al. 2003; Belokurov et al. 2006; Law & Majewski 2010). Compensating for the low [Fe/H] of its associated stellar stream ($\langle[Fe/H]\rangle = -1.07$; gray dashed line in Figure 4) and the mass lost throughout its interaction with the Milky Way (e.g., Ibata et al. 1997) should reconcile it with the MZR. Contrary to Sgr dSph, the GSE falls below the MZR of Kirby et al. (2013) due to its lower mean metallicity, despite having a $M_\star$ in between those of SMC and LMC. Such a discrepancy between $M_\star$ and ⟨[Fe/H]⟩ of GSE and its present-day counterparts can be attributed to the extended duration of star formation experienced by this pair of galaxies, including recent bursts (Nidever et al. 2020; Ruiz-Lara et al. 2020; Hasselquist et al. 2021; Massana et al. 2022); see the discussion regarding the redshift evolution of the MZR by Feuillet et al. (2020) and its impact on the interpretation of accreted populations. Unlike the surviving satellites, the star formation in GSE was likely abruptly quenched due to its own merging with the Milky Way, a scenario supported by the truncated age ($\gtrsim$8 Gyr) distribution of its stars (Gallart et al. 2019; Montalbán et al. 2021).

4. GSE Characterized by GCs

4.1. Candidates in the Literature

The first attempt at vetting GCs of GSE was conducted by Myeong et al. (2018c). These authors demonstrated that GCs of GSE, selected from dynamics alone, follow a track in AMR clearly separated from their in situ counterparts, being more metal-poor within the same age interval (data from Forbes & Bridges 2010). These results were confirmed and expanded with new DRs from Gaia by many subsequent studies (Massari et al. 2019; Forbes 2020; Horta et al. 2020; Kruijssen et al. 2020; Callingham et al. 2022).

Leveraging these various lists of candidates, we search APOGEE DR17 for GCs potentially associated with GSE. Within our initial sample of candidate GSE GCs with available APOGEE data, most were attributed to GSE by all aforementioned authors. One example of exception is NGC 5904, tentatively linked to a different accreted substructure, the so-called "Helmi streams" (Helmi et al. 1999; also Koppelman et al. 2019b and Limberg et al. 2021b). Indeed, we verified that the kinematic signature of this GC disfavors its connection with GSE (Section 4.3). Another, and more important, contested membership (between GSE and Sequoia) is that of ωCen. This GC contains an enormous metallicity spread (bottom panel of Figure 3; Table 1) and has long been suspected to be the stripped NSC of an accreted dwarf galaxy (e.g., Lee et al. 1999). Given the NSC nature of ωCen, solving this ambiguity can provide valuable constraints to dynamical models of the disruption of its host galaxy (e.g., Bekki & Freeman 2003).

4.2. The Case of ωCen and NGC 1851

Initially, Myeong et al. (2019) argued that ωCen should be associated with Sequoia on the basis of its location in the action-space diagram (top panel of Figure 3). On the other hand, Massari et al. (2019) prioritized an association with GSE due to the low binding energy of ωCen in comparison to other GSE GCs (right panel of Figure 5); being located at the core of the accreted galaxy, it would be expected to sink deeper into the potential of the Milky Way (Bekki & Freeman 2003). The contradiction between these scenarios was revisited by Forbes (2020) who favored the hypothesis of ωCen being the NSC of Sequoia instead of GSE. The main rationale for this conclusion was that a different Galactic GC should be the remaining nucleus of GSE, namely NGC 1851 (see also Tautvaišienė et al. 2022), due to its peculiar chemical composition (including an [Fe/H] spread of ∼0.07 dex; Carretta et al. 2011) combined with an apparently unequivocal dynamical connection in all works listed in Section 4.1. However, Pfeffer et al. (2021) performed a critical assessment of such claims and concluded that NGC 1851 is not a strong candidate for a NSC due its metallicity spread being so small and still contested; Villanova et al. (2010) found no evidence for an intrinsic [Fe/H] dispersion within the uncertainties. Recently, Callingham et al. (2022) used all available information (dynamics+metallicities +ages; Kruijssen et al. 2019b) to classify Galactic GCs and found an almost certain GSE membership for ωCen.

Assuming that ωCen and NGC 1851 are surviving NSCs, it is possible to calculate the $M_\star$ of their now-destroyed original galaxies from scaling relations between compact stellar nuclei and their host systems (Ferrarese et al. 2006; Rossa et al. 2006). Such an exercise was conducted by Sánchez-Janssen et al. (2019) for ωCen. These authors found $M_\star \sim 6 \times 10^8 M_\odot$ for the progenitor of this GC, which is, indeed, consistent with some estimates for GSE (e.g., Helmi et al. 2018). Here, we apply the most up-to-date, to the best of our knowledge, scaling relation between the mass of NSCs and $M_\star$ of their host galaxies (from the review of Neumayer et al. 2020; Equation 2) to predict the $M_\star$ of GSE in each case, either ωCen or NGC 1851 as its NSC. Their provided equation is reproduced below, but with terms

Table 1
GSE GCs with Available APOGEE DR17 Data

Name	R.A. (deg)	Decl. (deg)	$d_{\odot}$[a] (kpc)	$PM_{R.A.}$ (mas yr^{-1})	$PM_{Decl.}$ (mas yr^{-1})	v_{los} (km s^{-1})	N	$\langle$[Fe/H]$\rangle$	$\sigma_{[Fe/H]}$
NGC 288	13.19	−26.58	8.92 ± 0.09	4.16 ± 0.02	-5.71 ± 0.02	-44.5 ± 0.1	37	$-1.27^{+0.01}_{-0.01}$	$0.05^{+0.01}_{-0.01}$
NGC 362	15.81	−70.85	8.76 ± 0.10	6.69 ± 0.02	-2.54 ± 0.02	223.1 ± 0.3	37	$-1.11^{+0.01}_{-0.01}$	$0.04^{+0.01}_{-0.00}$
NGC 1851	78.53	−40.05	12.06 ± 0.13	2.14 ± 0.02	-0.65 ± 0.02	321.4 ± 1.6	24	$-1.10^{+0.01}_{-0.01}$	$0.05^{+0.01}_{-0.01}$
NGC 1904	81.04	−24.52	13.20 ± 0.17	2.47 ± 0.03	-1.59 ± 0.03	205.8 ± 0.2	22	$-1.51^{+0.02}_{-0.02}$	$0.07^{+0.01}_{-0.01}$
NGC 2298	102.25	−36.01	10.21 ± 0.13	3.32 ± 0.03	-2.18 ± 0.03	147.2 ± 0.6	5	$-1.84^{+0.04}_{-0.04}$	$0.09^{+0.06}_{-0.03}$
NGC 2808	138.01	−64.86	10.16 ± 0.16	0.99 ± 0.02	0.27 ± 0.02	103.6 ± 0.3	66	$-1.09^{+0.01}_{-0.01}$	$0.05^{+0.01}_{-0.00}$
NGC 6229	251.74	47.53	30.37 ± 0.45	-1.17 ± 0.03	-0.47 ± 0.03	-137.9 ± 0.7	3	$-1.27^{+0.03}_{-0.03}$	$0.04^{+0.09}_{-0.02}$
NGC 6341	259.28	43.14	8.60 ± 0.05	-4.94 ± 0.02	-0.62 ± 0.02	-120.6 ± 0.3	3	$-2.21^{+0.02}_{-0.02}$	$0.02^{+0.06}_{-0.02}$
NGC 7089	323.36	−0.82	11.62 ± 0.13	3.43 ± 0.03	-2.16 ± 0.02	3.8 ± 0.3	19	$-1.46^{+0.02}_{-0.02}$	$0.07^{+0.01}_{-0.01}$
ωCen	201.70	−47.48	5.49 ± 0.05	-3.25 ± 0.02	-6.75 ± 0.02	232.8 ± 0.2	571	$-1.61^{+0.01}_{-0.01}$	$0.20^{+0.01}_{-0.01}$

Note.
[a] Literature values (Section 4).

rearranged for convenience.

$$\log(M_{\star\,\text{host galaxy}}) = \frac{\log(M_{\text{NSC}}) - 6.51}{0.48} + 9, \quad (2)$$

where $M_{\star\,\text{host galaxy}}$ is the host galaxy's $M_{\star}$ and M_{NSC} is the mass of its corresponding NSC.

The adopted mass for ωCen is $3.64 \pm 0.04 \times 10^6$, recently estimated by Baumgardt & Hilker (2018) and revised as of 2021.[11] The mass of this GC translates into $M_{\star\,\text{host galaxy}} \approx 1.3 \times 10^9 M_{\odot}$ for its former host galaxy. Such $M_{\star}$ value is well within the literature range for GSE (see Figure 6) and is more than 10 times larger than the expected value for Sequoia of ~ 5–$8 \times 10^7 M_{\odot}$ (Myeong et al. 2019; Forbes 2020; Kruijssen et al. 2020; Callingham et al. 2022). Following this line of thought, it would be natural to imagine GSE as a stronger candidate as the host of such a robust NSC. Moreover, it is known that ωCen has experienced severe tidal stripping, including the formation of a long stellar stream (Ibata et al. 2019a, 2019b; see also Simpson et al. 2020). According to these authors' best model, ωCen has already lost ∼20% of its original mass. Despite the large scatter shown in Figure 6, there are no NSCs that are as massive as, or more than, ωCen within the literature range for the $M_{\star}$ of Sequoia, but we note the presence of some extreme outliers below this interval.

Regarding NGC 1851, its mass is $3.18 \pm 0.04 \times 10^5$ (Baumgardt & Hilker 2018, 2021 version). Using this value as input to Equation (2) gives $M_{\star\,\text{host galaxy}} \approx 8.0 \times 10^6 M_{\odot}$. This predicted $M_{\star}$ for the former host of NGC 1851, assuming this GC truly is a stripped NSC, is $\sim 1/100$ the expected value for GSE (Helmi et al. 2018; Feuillet et al. 2020; Forbes 2020). Within the literature $M_{\star}$ range of GSE, the fraction of NSCs as massive as, or less than, NGC 1851 is below 3%.

One of the defining features that differentiates canonical GCs from dwarf galaxies is their small [Fe/H] spreads (Willman & Strader 2012). Here, we utilize APOGEE DR17 data to investigate the claims of [Fe/H] variations within NGC 1851. In order to robustly derive the mean and intrinsic scatter ($\sigma_{[Fe/H]}$) of this GC's MDF, we model it as a Gaussian distribution, including Gaussian [Fe/H] measurement errors for individual stars. We implement a Markov Chain Monte Carlo (MCMC) strategy with the `emcee` package (Foreman-Mackey et al. 2013) to generate posterior distributions of both $\langle$[Fe/H]$\rangle$ and $\sigma_{[Fe/H]}$. The two-term Gaussian likelihood function adopted is identical to the one from Li et al. (2017) and is written as

$$\log\mathcal{L} = -\frac{1}{2}\sum_{i=1}^{N}\left[\log(\sigma^2_{[Fe/H]} + \sigma_i^2) + \frac{([Fe/H]_i - \langle[Fe/H]\rangle)^2}{(\sigma^2_{[Fe/H]} + \sigma_i^2)}\right], \quad (3)$$

where $[Fe/H]_i$ and σ_i are the iron-to-hydrogen ratio and its associated uncertainty, respectively, for a given ith star in a GC with N members. The uniform prior ranges are $-2.5 < \langle[Fe/H]\rangle < -0.5$ and nonnegative $\sigma_{[Fe/H]}$ values. As in Wan et al. (2020), the MCMC sampler is ran with 100 walkers and 1,000 steps, including a burn-in stage of 500.

We calculated $\langle[Fe/H]\rangle = -1.10^{+0.01}_{-0.01}$ and $\sigma_{[Fe/H]} = 0.05^{+0.01}_{-0.01}$ for NGC 1851, where lower and upper limits are 16th and 84th percentiles, respectively (Table 1). This $\sigma_{[Fe/H]}$ value is, indeed, larger than the reported errors. However, we applied the same method to other GCs listed in Section 4.1 with reasonable amount ($\geqslant 5$) of stars and also obtained similarly nonzero $\sigma_{[Fe/H]}$ (0.04–0.09 dex; Table 1). This result could be an artifact of underestimated abundance uncertainties. In fact, upon (re)analyzing APOGEE spectra (with photometric T_{eff} values), Masseron et al. (2019) and Mészáros et al. (2021) achieved uncertainties at the level of ∼0.1 dex for [Fe/H]. In any case, these results imply that NGC 1851 is not particularly special, i.e., according to our inspection, there is no evidence that this Galactic GC should be considered a candidate for NSC, in agreement with Pfeffer et al. (2021). We note that Mészáros et al. (2020) found no intrinsic [Fe/H] scatter in NGC 1851 in their own study with APOGEE DR17 data, but also recalibrated with photometric T_{eff}. As a sanity check, we applied our MCMC method to this sample of stars from NGC 1851 and confirmed that its $\sigma_{[Fe/H]} = 0.07^{+0.02}_{-0.02}$ is smaller than typical errors (0.10 dex). For reference, performing the same exercise for ωCen yields $\langle[Fe/H]\rangle = -1.61^{+0.01}_{-0.01}$ and $\sigma_{[Fe/H]} = 0.20^{+0.01}_{-0.01}$, which is comparable to the MDF obtained for this GC by Johnson & Pilachowski (2010; our Figure 3). Finally, a scenario where NGC 1851 is the NSC of GSE would need to be reconciled with the higher orbital energy of this GC in comparison with other members of this substructure (right

[11] https://people.smp.uq.edu.au/HolgerBaumgardt/globular/

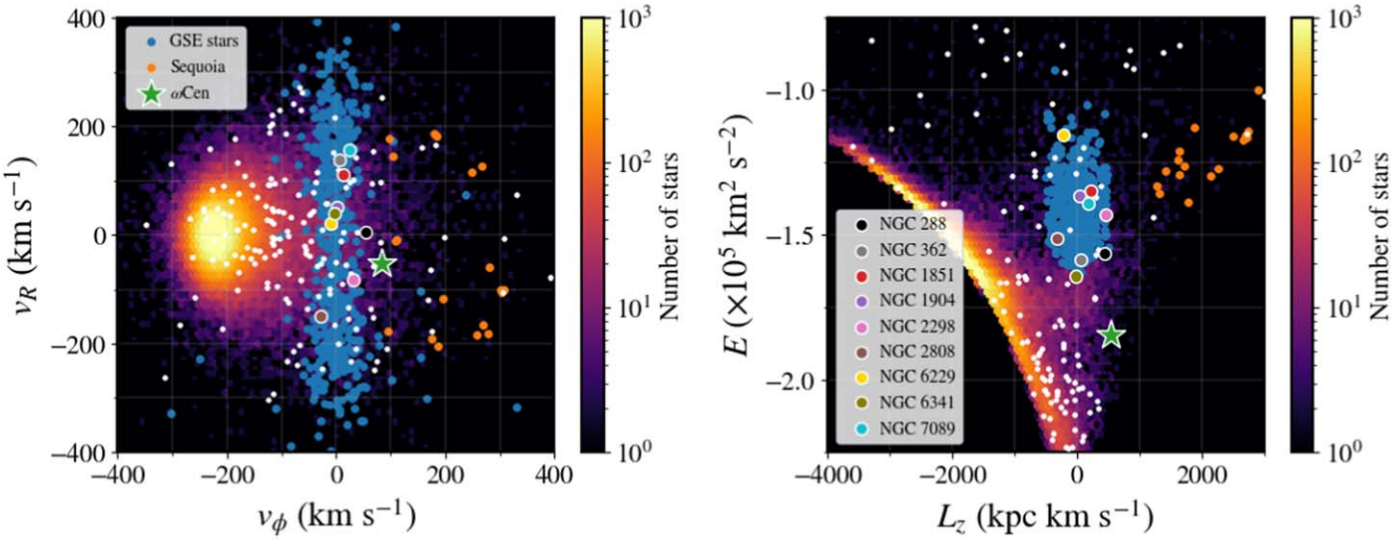

Figure 5. Left: (v_ϕ, v_R), where v_ϕ and v_R are the azimuthal and radial components (i.e., cylindrical coordinates) of the velocity vector, respectively. Right: (L_z, E). Blue and orange dots are GSE and Sequoia stars, respectively. White dots are Galactic GCs from the catalog of Vasiliev & Baumgardt (2021) with no observed stars in APOGEE DR17 or not associated with GSE at all. Colored symbols with white borders are confident (Section 4.3) GSE GC candidates .

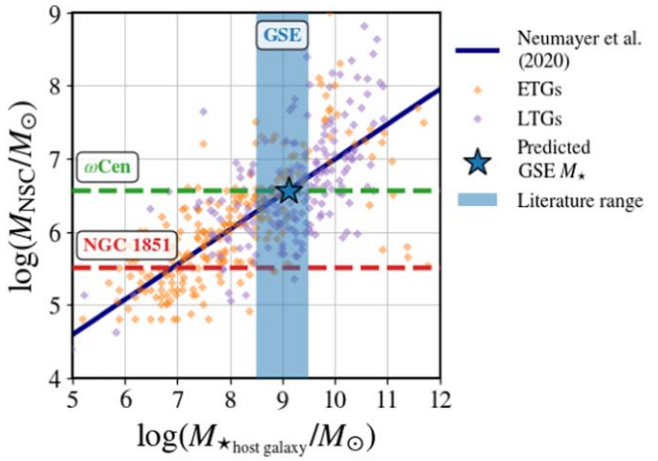

Figure 6. M_{NSC} vs. $M_{\star\ \mathrm{host\ galaxy}}$. Early- and late-type galaxies (ETGs and LTGs) from the recent compilation of Neumayer et al. (2020) are exhibited as orange and purple diamonds, respectively. The fit to these data is also shown (dark blue line; Equation (2)). The blue stripe covers the $M_\star$ range for GSE; $8.5 \leqslant \log(M_\star/M_\odot) \leqslant 9.5$ (see text). Finally, the blue star marker showcases the predicted $M_\star$ for GSE obtained from this relation. Dashed lines exhibit the masses (Baumgardt & Hilker 2018), updated as of 2021, of both ωCen (green) and NGC 1851 (red).

panel of Figure 5). Therefore, throughout the remainder of this paper, we consider NGC 1851 as a regular GC (Sections 4.3 and 4.4) and proceed with the interpretation that GSE is the best available candidate for the original host galaxy of ωCen.

4.3. Membership Probabilities

In order to confirm which GCs are the most likely to belong to GSE, we carried out a membership analysis considering all the available information. In Figure 7, we inspect the velocity (v_ϕ versus v_R) and integrals-of-motion (L_z versus E) planes. Once the GSE is well defined in these spaces, using the chemodynamical criteria adopted in this work for field stars (Section 3.1), we employ the region limited by those stars as our confidence region to compute the membership probabilities.

In Figure 7, the dots are GCs color-coded by their attributed membership probabilities, and the gray shaded area bounded by the black dotted line is the locus constructed from the chemodynamical selection (Equation (1)) of field stars (Figure 5). To construct this confidence region, we create a sample of 100 MC simulations for each field star from the uncertainties in v_ϕ, v_R, L_z, and E. With this sample, we binned the vertical axis in both planes (v_R and E; left and right panels, respectively) and computed the maximum and minimum values in the associated horizontal axes (i.e., v_ϕ and L_z) for each bin. This confidence region was created to give a probability of 100% for the GSE field stars. For each GC, we generated 100 MC realizations considering all four parameters. The final likelihood, $\mathcal{P}_{GSE}$, is given by the simultaneous fraction of realizations inside both delimited regions (colors in Figure 7). We observe that some of the GCs located close to the boundaries have probabilities of slightly over 10%; this is because these GCs have large error bars in their kinematic–dynamical parameters. Then, we considered as confident GSE members those GCs with a final membership probability $\mathcal{P}_{GSE} > 70\%$, resulting in a list of 19 GCs associated with this substructure (Table 2).

4.4. Age–Metallicity Relation (AMR)

The GSE AMR of Forbes (2020) was derived assuming the ages and metallicities taken from the literature that were measured from a variety of methods and data sets. Here, we provide a new GSE AMR using a statistical age determination and metallicities from high-resolution spectroscopy of the most probable GSE GCs. We obtained chemical information for GCs in APOGEE DR17, and, after calculating $\mathcal{P}_{GSE}$ for each of them, only nine survived the membership cut adopted ($\mathcal{P}_{GSE} > 70\%$). Those are NGC 288, NGC 362, NGC 1851, NGC 1904, NGC 2298, NGC 2808, NGC 6229, NGC 6341, and NGC 7089. We note that the Gaia EDR3 CMD of NGC 6229 has no clear main-sequence turnoff. Hence, we decided to exclude this cluster from further analyses.

With the goal of estimating a new AMR for GSE from the eight remaining APOGEE GCs, we recalculated, in a self-

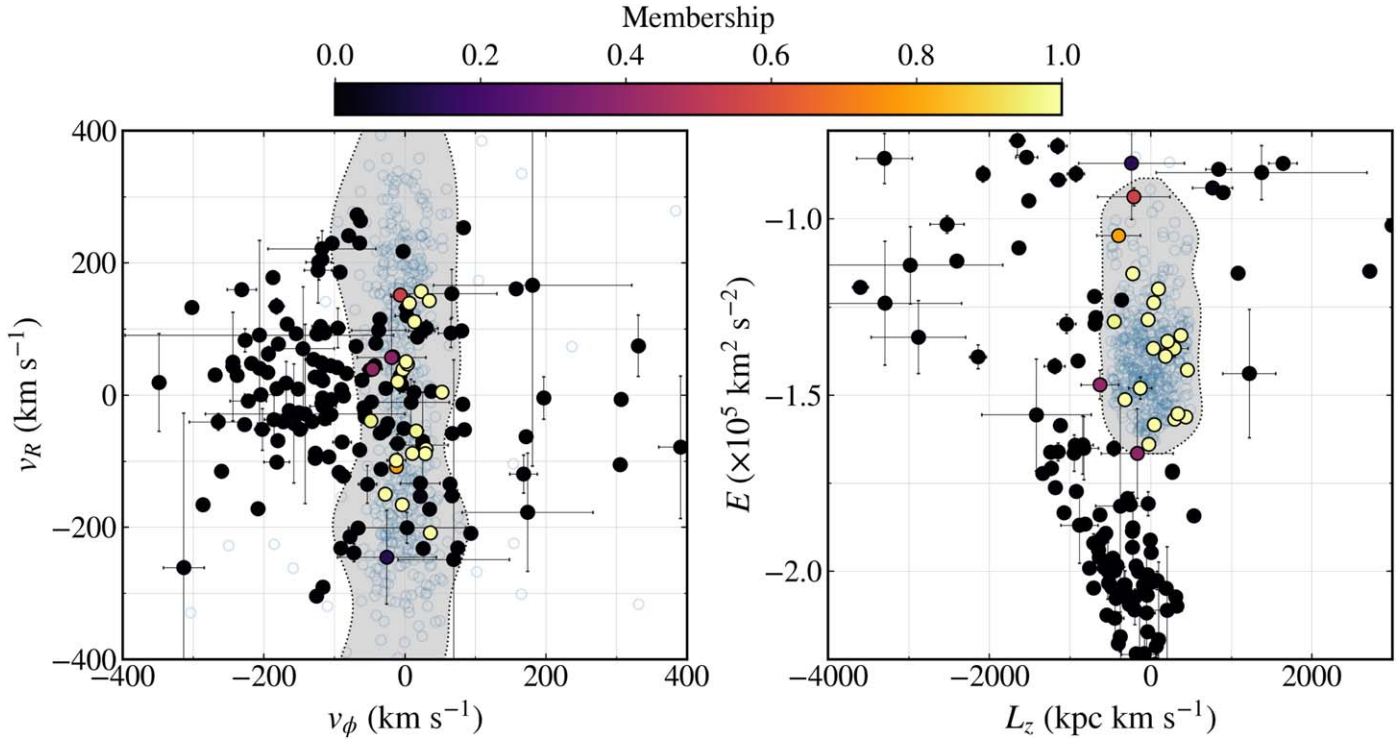

Figure 7. Membership probability of the GCs based on kinematic criteria (left panel) and integrals of motion (right panel) simultaneously. The gray area delineates the regions populated by GSE stars as shown with blue dots in Figure 5.

Table 2
Ages and [Fe/H] Values for GCs That Belong to GSE According to the Classification of Section 4.3 and Figure 7

Name	Kruijssen et al. (2019b)		This work	
	Age (Gyr)	[Fe/H]	Age (Gyr)	[Fe/H]
NGC 288	11.5 ± 0.4	-1.29 ± 0.11	11.9 ± 0.4	-1.28 ± 0.04
NGC 362	10.9 ± 0.4	-1.23 ± 0.10	10.5 ± 0.3	-1.11 ± 0.03
NGC 1261	10.8 ± 0.4	-1.23 ± 0.11	...	...
NGC 1851	10.5 ± 0.6	-1.10 ± 0.07	10.9 ± 0.3	-1.10 ± 0.03
NGC 1904	11.1 ± 0.9	-1.37 ± 0.10	12.3 ± 0.4	-1.51 ± 0.03
NGC 2298	12.8 ± 0.6	-1.80 ± 0.09	13.6 ± 0.4	-1.85 ± 0.06
NGC 2808	10.9 ± 0.6	-1.14 ± 0.03	11.5 ± 0.4	-1.09 ± 0.05
NGC 4147	12.1 ± 0.5	-1.66 ± 0.12	...	...
NGC 5286	12.7 ± 0.5	-1.60 ± 0.14	...	...
NGC 5634	11.8 ± 0.5	-1.94 ± 0.10	...	...
NGC 6229[a]	...	...	...	...
NGC 6341	13.0 ± 0.5	-2.30 ± 0.10	13.3 ± 0.4	-2.21 ± 0.03
NGC 6779	13.3 ± 0.5	-2.07 ± 0.09	...	...
NGC 6864	9.9 ± 0.5	-1.03 ± 0.10	...	...
NGC 6981	11.7 ± 0.4	-1.40 ± 0.13	...	...
NGC 7089	12.0 ± 0.5	-1.52 ± 0.15	11.5 ± 0.3	-1.47 ± 0.05
NGC 7492	12.0 ± 1.4	-1.41 ± 0.10	...	...
IC 1257	...	...	...	...
Pal 2	...	...	...	...

Note. Left columns are the parameters derived by Kruijssen et al. (2019b), while the rightmost ones present the values of ages and [Fe/H] derived through the isochrone fitting.
[a] Not enough information from Gaia EDR3 to provide a good isochrone fitting (see text).

consistent way, their fundamental parameters (ages, $d_\odot$, and reddening) via isochrone fitting. We utilized the Gaia EDR3 public catalog from Vasiliev & Baumgardt (2021) to compile the necessary photometric data. After that, we constructed the CMD for each GC considering only those stars with a membership probability >99% (Section 2.2). Furthermore, we employed the `SIRIUS` code (Souza et al. 2020) adapted to perform the isochrone fitting following a Bayesian approach to obtain the posterior distribution of the parameters. For instance, we imposed a prior to the metallicity distribution adopting the [Fe/H] values from APOGEE. We discuss the results from the isochrone fitting itself in Appendix B and report them in the rightmost columns of Table 2.

We adopt the model of Forbes (2020) to fit the AMR:

$$Z = -p \ln\left(\frac{t}{t_f}\right), \tag{4}$$

where Z is the metallicity in the form of mass fraction, p is the effective yield, and t_f is the look-back time since the initial formation of the system. The AMR is highly sensitive to variations in age, mainly for its old-age portion. Note that, at a certain age value, there exists a *knee* separating the almost linearly declining sequence of comparatively young GCs from the asymptotic regime of old ones. Our best fit for the AMR is presented in Figure 8; $p = 0.33 \pm 0.05$ and $t_f = 13.60 \pm 0.11$ Gyr. This AMR is in good agreement with that of Forbes (2020, $p = 0.27 \pm 0.02$ and $t_f = 13.55 \pm 0.10$ Gyr). Although the AMR parameters are compatible within errors, our p determination is slightly higher than that from these authors'. The reason for this behavior is APOGEE metallicities being, in some cases, higher than those adopted by Kruijssen et al. (2019b; our Table 2). Additionally, as expected, the old-metal-rich component of in situ GCs is dominated by those with probabilities around zero.

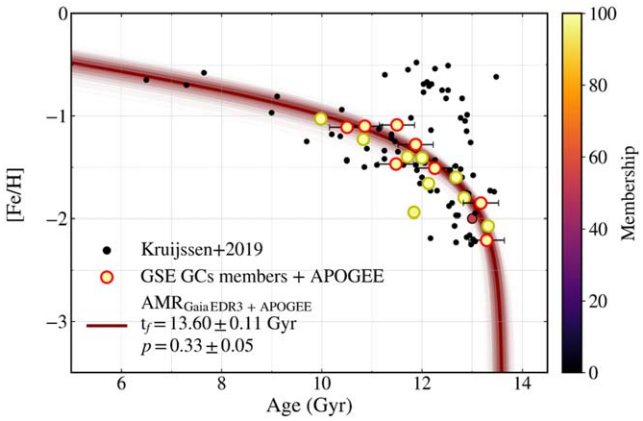

Figure 8. AMR fitting for the GSE GCs with APOGEE and Gaia EDR3 data. The dots are colored according to their membership probability ($\mathcal{P}_{\rm GSE}$) values. The dots with red edges represent the GSE GCs with information from APOGEE. For those GCs, we recalculated their ages (Table 2). The GCs without APOGEE data, however, with $\mathcal{P}_{\rm GSE} > 70\%$, are colored with yellow edges. To size the dots, we also used the $\mathcal{P}_{\rm GSE}$. The red solid line is the best-fit AMR to the former sample. The red shaded region indicates the AMRs constructed using MC sampling from the uncertainties in both ages and [Fe/H] values.

5. Conclusions

In this work, we combined the APOGEE DR17 (spectroscopic) and Gaia EDR3 (photometric and astrometric) data sets with the purpose of characterizing, in a self-consistent manner, the stellar and GC populations of GSE. With this information at hand, we assembled a novel set of criteria to select the genuine GSE member stars. With the aid of chemical-evolution models, this sample was utilized to interpret the overall abundance patterns of GSE in comparison with the Milky Way's disk(s) as well as its surviving satellites. Furthermore, the kinematic–dynamical signature of GSE field stars allowed us to construct a list of Galactic GCs confidently associated with this substructure from a robust membership analysis. We also recalculated the fundamental parameters for GSE GCs (ages, $d_\odot$, and reddening) via statistical isochrone fitting taking into account informative [Fe/H] priors from available APOGEE observations. The main results are summarized below.

1. Our new chemodynamical selection of GSE stars (Equation (1)) defines a narrower MDF in comparison to the merely dynamical criteria (Feuillet et al. 2020) thanks to the removal of contamination from disk stars. The final median [Fe/H] of GSE is -1.22 with a MAD of 0.23 dex.
2. In [Mg/Fe]–[Fe/H], GSE stars constitute a declining sequence within $-1.5 \lesssim$ [Fe/H] < -0.7. Differently from Sgr dSph, SMC, and LMC, the distribution of [Mg/Fe] for GSE shows neither increase nor flattening toward the metal-rich regime, indicative of a single-burst star formation history.
3. Within this [Fe/H] interval, GSE has higher $\langle$[Mg/Mn]$\rangle$ and $\langle$[Al/Fe]$\rangle$ in comparison to Sgr dSph, SMC, and LMC. This feature can be explained by the extended chemical-enrichment histories of present-day Milky Way satellites as well as a higher SFE for GSE prior to its merger.
4. Unlike these surviving dwarfs, Sequoia overlaps with GSE in all abundance planes, but being more metal-poor. Hence, this population's MDF does not track GSE's as closely as previously suggested (Naidu et al. 2020, 2021). If these substructures are truly connected, this would translate into a steeper [Fe/H] gradient for their progenitor galaxy.
5. GSE has a lower $\langle$[Fe/H]$\rangle$ than both SMC and LMC, but with a $M_\star$ in between them, in agreement with the expectation that its star formation—chemical-evolution history was interrupted at early times.
6. We found $M_{\star\ \rm host\ galaxy} \approx 1.3 \times 10^9 M_\odot$ for the progenitor of ωCen, which is well within literature expectations for GSE.
7. Assuming NGC 1851 as a stripped NSC, we found $M_{\star\ \rm host\ galaxy} \approx 8.0 \times 10^6 M_\odot$, which is $\sim$1/100 the expected mass for GSE.
8. We calculated $\sigma_{\rm [Fe/H]}$ for GCs with APOGEE data. We found no evidence of an atypical metallicity spread in NGC 1851; unlike ωCen, its measured $\sigma_{\rm [Fe/H]}$ is at the level of other GCs. Therefore, we do not consider NGC 1851 a stripped NSC.
9. A scenario where NGC 1851 is a NSC would need to be reconciled with its orbital energy being higher than other GCs of GSE. We favor the interpretation that GSE is the best available candidate for the original host galaxy of ωCen.
10. We carried out a membership analysis for candidate GCs of GSE considering the kinematics and dynamics. We consolidated a list of 19 GCs confidently ($\mathcal{P}_{\rm GSE} > 70\%$) associated it.
11. We obtained fundamental parameters (including ages) for eight GSE GCs via isochrone fitting from Gaia EDR3 photometry and APOGEE [Fe/H] priors. Then, we modeled the AMR of GSE. Our best-fit parameters ($p = 0.33 \pm 0.05$ and $t_f = 13.60 \pm 0.11$ Gyr) are broadly consistent with previous results (Forbes 2020).

The advent of precise photometric and astrometric data for more than a billion stars thanks to the Gaia space mission has revolutionized our understanding of the formation and evolution of the Milky Way. In combination with chemical abundances provided by high-resolution spectroscopic surveys, we have started to disentangle the sequence of merging events that happened throughout the history of the Galaxy. This work provides a demonstration that the currently available information allows us to reconstruct the properties of dwarf galaxies accreted by the Milky Way in the past. Nevertheless, it has become clear that the stellar and GC populations need to be taken into account in order for us to obtain the full picture for these systems. Hence, the self-consistent framework established here highlights how homogeneous data sets for field and GC stars alike can be leveraged for the task of constraining the properties of now-destroyed ancient dwarf galaxies.

We thank the anonymous referee for a timely and constructive report. We also thank Nadine Neumayer and Torsten Böker for assistance with NSC data and Szabolcs Mészáros for readily providing access to the results on ωCen from reanalyzed APOGEE spectra. G.L. acknowledges CAPES/PROEX (Proc. 88887.481172/2020-00) and FAPESP (Proc. 2021/10429-0). S.O.S. acknowledges FAPESP (Proc. 2018/22044-3) and the support of the Deutsche Forschungsgemeinschaft (DFG, project number: 428473034). A.P.-V. and S.O.S. acknowledge the DGAPA-PAPIIT grant IA103122. S.R. is thankful for support from FAPESP (Proc. 2015/50374-0 and Proc. 2014/18100-4),

CAPES, and CNPq. H.D.P. thanks FAPESP (Proc. 2018/21250-9). R.M.S. acknowledges CNPq (Proc. 306667/2020-7). G.L., S.R., H.D.P., and R.M.S. extend heartfelt thanks to all involved with the "Brazilian Milky Way group meeting," in particular João A. Amarante, Hélio J. Rocha-Pinto, Leandro Beraldo e Silva, and Fabrícia O. Barbosa. Conversations within this space inspired the original concept for this paper. G.L. and S.R. are grateful toward Katia Cunha for tips on the metal-poor end of APOGEE data. G.L. also thanks Pedro H. Cezar and Catarina P. Aydar for discussions regarding aspects of galaxy evolution. Finally, G.L. acknowledges researchers within the Galactic-archeology community who provided feedback on a preprint version of this article, in particular GyuChul Myeong and Rohan P. Naidu.

This work has made use of data from the European Space Agency (ESA) mission Gaia (https://www.cosmos.esa.int/gaia), processed by the Gaia Data Processing and Analysis Consortium (DPAC, https://www.cosmos.esa.int/web/gaia/dpac/consortium). Funding for the DPAC has been provided by national institutions, in particular the institutions participating in the Gaia Multilateral Agreement.

Funding for the Sloan Digital Sky Survey IV has been provided by the Alfred P. Sloan Foundation, the U.S. Department of Energy Office of Science, and the participating institutions. SDSS-IV acknowledges support and resources from the Center for High Performance Computing at the University of Utah. The SDSS website is www.sdss.org. SDSS-IV is managed by the Astrophysical Research Consortium for the Participating Institutions of the SDSS Collaboration.

This research has made use of the VizieR catalog access tool, Centre de Données astronomiques de Strasbourg, Strasbourg, France (https://cds.u-strasbg.fr). The original description of the VizieR service was published in Ochsenbein et al. (2000).

This research has been conducted despite the ongoing dismantling of the Brazilian scientific system.

Software: `Astropy` (Astropy Collaboration et al. 2013, 2018), `corner` (Foreman-Mackey 2016), `matplotlib` (Hunter 2007), `NumPy` (van der Walt et al. 2011), `pandas` (McKinney 2010), `SciPy` (Virtanen et al. 2020), `scikit-learn` (Pedregosa et al. 2012), `TOPCAT` (Taylor 2005).

Appendix A
Details on Chemical-evolution Models

In this appendix, we provide further details regarding the chemical-evolution trajectories computed with the `flexCE` code and presented in Section 3.3 and Figure 2. Although similar calculations were originally described in Horta et al. (2021), our goal is to make this information easily accessible and comprehensible for the interested reader, in particular regarding the quantitative differences between "accreted" and " in situ" models.

All tracks were calculated within a one-zone, open-box (i.e., allowing for gas inflows and outflows) framework under the assumption of instantaneous and complete mixing. The standard (in `flexCE`) exponentially decaying inflow law was adopted. The computations started from the same initial chemical compositions and were conducted in time steps of 10 Myr for a total of 13.5 Gyr. The initial mass function is from Kroupa (2001), and the stellar mass range considered is between 0.1 and 100 $M_{\odot}$. Nucleosynthesis yields of core-collapse supernovae (Limongi & Chieffi 2006), single-degenerate (Chandrasekhar mass) type Ia supernovae (Iwamoto et al. 1999), and asymptotic giant branch stars (Karakas 2010) are accounted for, but see Andrews et al. (2017) for details on the process of interpolation and extrapolation of their mass and metallicity grids. The delay-time distribution of type Ia supernovae is an exponential with a characteristic timescale of 1.5 Gyr and minimum delay of 150 Myr, as recommended by Andrews et al. (2017).

The Milky Way–massive galaxy-like evolutionary track was originally constructed by Andrews et al. (2017, their so-called "fiducial" model) to reproduce the abundance trends of the solar neighborhood (within $\lesssim$200 pc from the Sun), in particular [O/Fe]–[Fe/H] (data from Ramírez et al. 2013). We highlight that there is a slight change in the SFE between the in situ trajectory of Horta et al. (2021; adopted by us) and the one from Andrews et al. (2017); SFE $= 1.5 \times 10^{-9}\,\mathrm{yr}^{-1}$ versus $1.0 \times 10^{-9}\,\mathrm{yr}^{-1}$, respectively. Other than that, these models are identical (see the Table 1 from both works). The set of quantities that effectively differentiate in situ from the accreted models are the initial gas masses ($2 \times 10^{10}\,M_{\odot}$ versus $3 \times 10^{9}\,M_{\odot}$, respectively), inflow masses ($3.5 \times 10^{11}\,M_{\odot}$ versus $6 \times 10^{10}\,M_{\odot}$) and timescales (6.0 versus 2.5 Gyr), outflow mass-loading factors (2.5 versus 6.0), and SFEs (the aforementioned 1.5×10^{-9} versus $1.0 \times 10^{-10}\,\mathrm{yr}^{-1}$). Finally, in Section 3.3 and Figure 2, we also presented our *low-SFE* variation of the accreted model, calculated with a SFE reduced by 80%, i.e., SFE $= 2.0 \times 10^{-11}\,\mathrm{yr}^{-1}$. We refer the reader to Andrews et al. (2017) for details on the exact parameterizations utilized in `flexCE` as well as Matteucci (2012) for a pedagogical introduction to notions of galactic chemical evolution.

Appendix B
Results of Isochrone Fitting

We employed the `SIRIUS` code (Souza et al. 2020) to perform the isochrone fitting. This code provides a Bayesian interpretation of the fundamental parameters age, reddening ($E(B-V)$), $d_{\odot}$, and metallicity ([Fe/H]). From the posterior distribution of each parameter, we can extract the best value as the medians and the errors from the 16th and 84th percentiles. The isochrone set employed is from Dartmouth Stellar Evolutionary Database (Dotter et al. 2008), computed for the Gaia photometric bands G, G_{BP}, and G_{RP}. We interpolate these models in age and [Fe/H] with the random values given by the algorithm. In principle, a simple box prior distribution was assumed for the age, avoiding the values outside the range 10–15 Gyr, and for distances, considering only $1 \leqslant d_{\odot}/\mathrm{kpc} \leqslant 20$. For [Fe/H], we assumed the MDFs from APOGEE as priors (Section 4.2/Table 1). Finally, only positive values of $E(B-V)$ are allowed. To convert the isochrone magnitudes into apparent ones, we adopted the extinction law with standard $R_V = 3.1$. Previous authors observed a variation of the extinction law in the direction of the Galactic bulge (Nataf et al. 2016; Pallanca et al. 2021; Souza et al. 2021), where its influence is highest, decreasing the R_V to 2.5. Once our GC sample is in a region with low extinction, we can adopt the conservative value of R_V.

For the purpose of visual inspection, the best-fit results are shown as blue solid lines in Figure 9 overlaid to the blue shaded 1σ regions. In general, the 1σ bands are able to describe the whole CMD for all clusters. We note that, for NGC 1851 and NGC 2808, the age and [Fe/H] are compatible with the literature (VandenBerg et al. 2013; Kruijssen et al. 2019b).

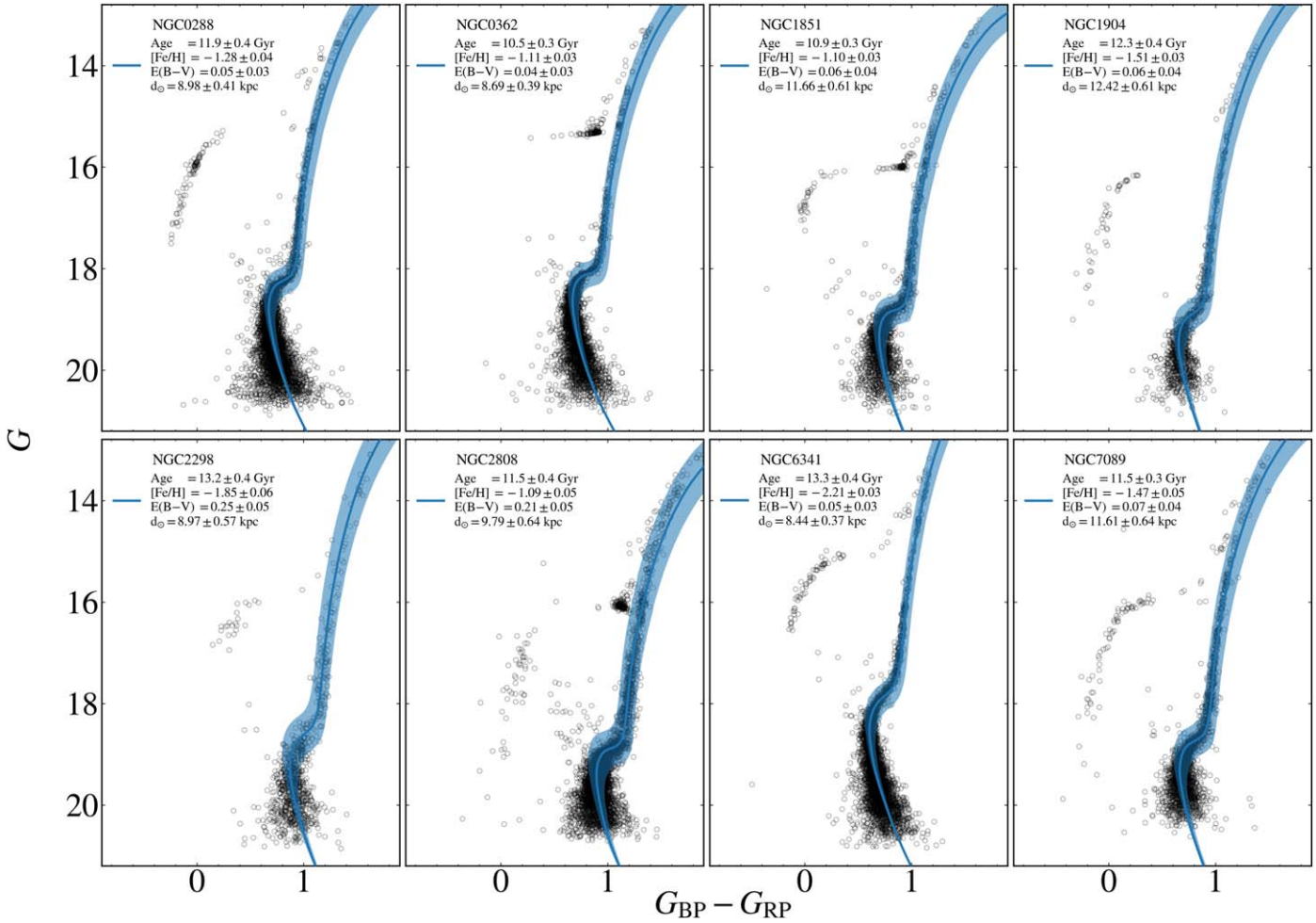

Figure 9. Gaia EDR3 CMDs for the GSE GCs with available APOGEE data. In each panel, the best-fit isochrone is the blue solid line, and the shaded area shows the region within 1σ for all parameters.

However, there is a discrepancy in their subgiant branch slopes. The reason for that is because both clusters are some of the most massive GCs (Baumgardt & Hilker 2018; Kruijssen et al. 2019b). Moreover, both GCs are host to multiple stellar populations (Milone et al. 2017). NGC 2808 harbors five stellar populations almost without [Fe/H] variations, classifying it as a type I GC (Milone et al. 2017). On the other hand, NGC 1851 is a type II GC as it hosts a poorly inhabited metal-rich stellar population (Milone et al. 2017). Even though the photometric tagging of multiple stellar populations is more efficient using ultraviolet passbands (Lee 2015; Piotto et al. 2015), for massive GCs, the variations in [Fe/H] (probably in age also) can allow the visual split of the main-sequence turnoff using optical passbands (Lee et al. 1999; Bedin et al. 2004).

ORCID iDs

Guilherme Limberg https://orcid.org/0000-0002-9269-8287
Stefano O. Souza https://orcid.org/0000-0001-8052-969X
Angeles Pérez-Villegas https://orcid.org/0000-0002-5974-3998
Silvia Rossi https://orcid.org/0000-0001-7479-5756
Hélio D. Perottoni https://orcid.org/0000-0002-0537-4146
Rafael M. Santucci https://orcid.org/0000-0002-7529-1442

References

Abdurro'uf, Accetta, K., Aerts, C., et al. 2022, ApJS, 259, 35
Abolfathi, B., Aguado, D. S., Aguilar, G., et al. 2018, ApJS, 235, 42
Aguado, D. S., Belokurov, V., Myeong, G. C., et al. 2021, ApJL, 908, L8
Amarante, J. A. S., Smith, M. C., & Boeche, C. 2020, MNRAS, 492, 3816
An, D., & Beers, T. C. 2021, ApJ, 907, 101
Anders, F., Khalatyan, A., Chiappini, C., et al. 2019, A&A, 628, A94
Andrews, B. H., Weinberg, D. H., Schönrich, R., & Johnson, J. A. 2017, ApJ, 835, 224
Astropy Collaboration, Price-Whelan, A. M., Sipőcz, B. M., et al. 2018, AJ, 156, 123
Astropy Collaboration, Robitaille, T. P., Tollerud, E. J., et al. 2013, A&A, 558, A33
Baumgardt, H., & Hilker, M. 2018, MNRAS, 478, 1520
Baumgardt, H., Hilker, M., Sollima, A., & Bellini, A. 2019, MNRAS, 482, 5138
Baumgardt, H., & Vasiliev, E. 2021, MNRAS, 505, 5957
Beaton, R. L., Oelkers, R. J., Hayes, C. R., et al. 2021, AJ, 162, 302
Bedin, L. R., Piotto, G., Anderson, J., et al. 2004, ApJL, 605, L125
Bekki, K., & Freeman, K. C. 2003, MNRAS, 346, L11
Belokurov, V., Erkal, D., Evans, N. W., Koposov, S. E., & Deason, A. J. 2018, MNRAS, 478, 611
Belokurov, V., Zucker, D. B., Evans, N. W., et al. 2006, ApJL, 642, L137
Bignone, L. A., Helmi, A., & Tissera, P. B. 2019, ApJL, 883, L5
Bland-Hawthorn, J., & Gerhard, O. 2016, ARA&A, 54, 529
Blumenthal, G. R., Faber, S. M., Primack, J. R., & Rees, M. J. 1984, Natur, 311, 517

Borsato, N. W., Martell, S. L., & Simpson, J. D. 2020, MNRAS, 492, 1370
Bovy, J. 2015, ApJS, 216, 29
Buder, S., Lind, K., Ness, M. K., et al. 2022, MNRAS, 510, 2407
Callingham, T. M., Cautun, M., Deason, A. J., et al. 2022, MNRAS, 513, 4107
Carollo, D., Beers, T. C., Lee, Y. S., et al. 2007, Natur, 450, 1020
Carollo, D., Beers, T. C., Chiba, M., et al. 2010, ApJ, 712, 692
Carretta, E., Lucatello, S., Gratton, R. G., Bragaglia, A., & D'Orazi, V. 2011, A&A, 533, A69
Chiba, M., & Beers, T. C. 2000, AJ, 119, 2843
Cioni, M. R. L. 2009, A&A, 506, 1137
Conroy, C., Bonaca, A., Cargile, P., et al. 2019, ApJ, 883, 107
Conselice, C. J. 2014, ARA&A, 52, 291
Das, P., Hawkins, K., & Jofré, P. 2020, MNRAS, 493, 5195
Deason, A. J., Belokurov, V., Koposov, S. E., & Lancaster, L. 2018, ApJL, 862, L1
Di Matteo, P., Haywood, M., Lehnert, M. D., et al. 2019, A&A, 632, A4
Dotter, A., Chaboyer, B., Jevremović, D., et al. 2008, ApJS, 178, 89
Elias, L. M., Sales, L. V., Helmi, A., & Hernquist, L. 2020, MNRAS, 495, 29
Faber, S. M., & Gallagher, J. S. 1979, ARA&A, 17, 135
Fabricius, C., Luri, X., Arenou, F., et al. 2021, A&A, 649, A5
Fattahi, A., Belokurov, V., Deason, A. J., et al. 2019, MNRAS, 484, 4471
Fernández-Alvar, E., Carigi, L., Schuster, W. J., et al. 2018, ApJ, 852, 50
Ferrarese, L., Côté, P., Dalla Bontà, E., et al. 2006, ApJL, 644, L21
Feuillet, D. K., Feltzing, S., Sahlholdt, C. L., & Casagrande, L. 2020, MNRAS, 497, 109
Forbes, D. A. 2020, MNRAS, 493, 847
Forbes, D. A., & Bridges, T. 2010, MNRAS, 404, 1203
Foreman-Mackey, D. 2016, JOSS, 1, 24
Foreman-Mackey, D., Hogg, D. W., Lang, D., & Goodman, J. 2013, PASP, 125, 306
Freeman, K., & Bland-Hawthorn, J. 2002, ARA&A, 40, 487
Gaia Collaboration, Prusti, T., de Bruijne, J. H. J., et al. 2016, A&A, 595, A1
Gaia Collaboration, Brown, A. G. A., Vallenari, A., et al. 2018a, A&A, 616, A1
Gaia Collaboration, Babusiaux, C., van Leeuwen, F., et al. 2018b, A&A, 616, A10
Gaia Collaboration, Katz, D., Antoja, T., et al. 2018c, A&A, 616, A11
Gaia Collaboration, Helmi, A., van Leeuwen, F., et al. 2018d, A&A, 616, A12
Gaia Collaboration, Brown, A. G. A., Vallenari, A., et al. 2021, A&A, 649, A1
Gallart, C., Bernard, E. J., Brook, C. B., et al. 2019, NatAs, 3, 932
Gallart, C., Zoccali, M., & Aparicio, A. 2005, ARA&A, 43, 387
García Pérez, A. E., Allende Prieto, C., Holtzman, J. A., et al. 2016, AJ, 151, 144
Grand, R. J. J., Kawata, D., Belokurov, V., et al. 2020, MNRAS, 497, 1603
Gravity Collaboration, Abuter, R., Amorim, A., et al. 2019, A&A, 625, L10
Gudin, D., Shank, D., Beers, T. C., et al. 2021, ApJ, 908, 79
Hasselquist, S., Hayes, C. R., Lian, J., et al. 2021, ApJ, 923, 172
Hawkins, K., Jofré, P., Masseron, T., & Gilmore, G. 2015, MNRAS, 453, 758
Hayden, M. R., Bovy, J., Holtzman, J. A., et al. 2015, ApJ, 808, 132
Hayes, C. R., Majewski, S. R., Shetrone, M., et al. 2018, ApJ, 852, 49
Hayes, C. R., Majewski, S. R., Hasselquist, S., et al. 2020, ApJ, 889, 63
Haywood, M., Di Matteo, P., Lehnert, M. D., et al. 2018, ApJ, 863, 113
Helmi, A. 2020, ARA&A, 58, 205
Helmi, A., Babusiaux, C., Koppelman, H. H., et al. 2018, Natur, 563, 85
Helmi, A., & White, S. D. M. 1999, MNRAS, 307, 495
Helmi, A., White, S. D. M., de Zeeuw, P. T., & Zhao, H. 1999, Natur, 402, 53
Ho, I. T., Kudritzki, R.-P., Kewley, L. J., et al. 2015, MNRAS, 448, 2030
Horta, D., Schiavon, R. P., Mackereth, J. T., et al. 2020, MNRAS, 493, 3363
Horta, D., Schiavon, R. P., Mackereth, J. T., et al. 2021, MNRAS, 500, 1385
Horta, D., Schiavon, R. P., Mackereth, J. T., et al. 2022, arXiv:2204.04233
Hunter, J. D. 2007, CSE, 9, 90
Ibata, R. A., Bellazzini, M., Malhan, K., Martin, N., & Bianchini, P. 2019a, NatAs, 3, 667
Ibata, R. A., Gilmore, G., & Irwin, M. J. 1994, Natur, 370, 194
Ibata, R. A., Gilmore, G., & Irwin, M. J. 1995, MNRAS, 277, 781
Ibata, R. A., Malhan, K., & Martin, N. F. 2019b, ApJ, 872, 152
Ibata, R. A., Wyse, R. F. G., Gilmore, G., Irwin, M. J., & Suntzeff, N. B. 1997, AJ, 113, 634
Iorio, G., & Belokurov, V. 2019, MNRAS, 482, 3868
Iorio, G., & Belokurov, V. 2021, MNRAS, 502, 5686
Iwamoto, K., Brachwitz, F., Nomoto, K., et al. 1999, ApJS, 125, 439
Johnson, C. I., & Pilachowski, C. A. 2010, ApJ, 722, 1373
Jönsson, H., Holtzman, J. A., Allende Prieto, C., et al. 2020, AJ, 160, 120
Karakas, A. I. 2010, MNRAS, 403, 1413
Kauffmann, G., White, S. D. M., & Guiderdoni, B. 1993, MNRAS, 264, 201
Kennicutt, R. C. J. 1998, ApJ, 498, 541
Kirby, E. N., Cohen, J. G., Guhathakurta, P., et al. 2013, ApJ, 779, 102
Kirby, E. N., Lanfranchi, G. A., Simon, J. D., Cohen, J. G., & Guhathakurta, P. 2011, ApJ, 727, 78
Koppelman, H., Helmi, A., & Veljanoski, J. 2018, ApJL, 860, L11
Koppelman, H. H., Bos, R. O. Y., & Helmi, A. 2020, A&A, 642, L18
Koppelman, H. H., Helmi, A., Massari, D., Price-Whelan, A. M., & Starkenburg, T. K. 2019a, A&A, 631, L9
Koppelman, H. H., Helmi, A., Massari, D., Roelenga, S., & Bastian, U. 2019b, A&A, 625, A5
Kroupa, P. 2001, MNRAS, 322, 231
Kruijssen, J. M. D., Pfeffer, J. L., Crain, R. A., & Bastian, N. 2019a, MNRAS, 486, 3134
Kruijssen, J. M. D., Pfeffer, J. L., Reina-Campos, M., Crain, R. A., & Bastian, N. 2019b, MNRAS, 486, 3180
Kruijssen, J. M. D., Pfeffer, J. L., Chevance, M., et al. 2020, MNRAS, 498, 2472
Lancaster, L., Koposov, S. E., Belokurov, V., Evans, N. W., & Deason, A. J. 2019, MNRAS, 486, 378
Lane, J. M. M., Bovy, J., & Mackereth, J. T. 2022, MNRAS, 510, 5119
Law, D. R., & Majewski, S. R. 2010, ApJ, 714, 229
Leaman, R., VandenBerg, D. A., & Mendel, J. T. 2013, MNRAS, 436, 122
Lee, J.-W. 2015, ApJS, 219, 7
Lee, Y. W., Joo, J. M., Sohn, Y. J., et al. 1999, Natur, 402, 55
Li, T. S., Simon, J. D., Drlica-Wagner, A., et al. 2017, ApJ, 838, 8
Limberg, G., Rossi, S., Beers, T. C., et al. 2021a, ApJ, 907, 10
Limberg, G., Santucci, R. M., Rossi, S., et al. 2021b, ApJL, 913, L28
Limongi, M., & Chieffi, A. 2006, ApJ, 647, 483
Lindegren, L., Klioner, S. A., Hernández, J., et al. 2021a, A&A, 649, A2
Lindegren, L., Bastian, U., Biermann, M., et al. 2021b, A&A, 649, A4
Ma, X., Hopkins, P. F., Faucher-Giguère, C.-A., et al. 2016, MNRAS, 456, 2140
Mackereth, J. T., Schiavon, R. P., Pfeffer, J., et al. 2019, MNRAS, 482, 3426
Majewski, S. R., Skrutskie, M. F., Weinberg, M. D., & Ostheimer, J. C. 2003, ApJ, 599, 1082
Majewski, S. R., Schiavon, R. P., Frinchaboy, P. M., et al. 2017, AJ, 154, 94
Massana, P., Ruiz-Lara, T., Noël, N. E. D., et al. 2022, MNRAS, 513, L40
Massari, D., Koppelman, H. H., & Helmi, A. 2019, A&A, 630, L4
Masseron, T., García-Hernández, D. A., Mészáros, S., et al. 2019, A&A, 622, A191
Matsuno, T., Aoki, W., & Suda, T. 2019, ApJL, 874, L35
Matsuno, T., Hirai, Y., Tarumi, Y., et al. 2021, A&A, 650, A110
Matsuno, T., Koppelman, H. H., Helmi, A., et al. 2022, A&A, 661, A103
Matteucci, F. 2012, Chemical Evolution of Galaxies (Berlin: Springer)
McConnachie, A. W. 2012, AJ, 144, 4
McKinney, W. 2010, in Proc. 9th Python in Science Conf., ed. S. van der Walt & J. Millman, 56
McMillan, P. J. 2017, MNRAS, 465, 76
McMillan, P. J., & Binney, J. J. 2008, MNRAS, 390, 429
Mészáros, S., Masseron, T., García-Hernández, D. A., et al. 2020, MNRAS, 492, 1641
Mészáros, S., Masseron, T., Fernández-Trincado, J. G., et al. 2021, MNRAS, 505, 1645
Milone, A. P., Piotto, G., Renzini, A., et al. 2017, MNRAS, 464, 3636
Montalbán, J., Mackereth, J. T., Miglio, A., et al. 2021, NatAs, 5, 640
Monty, S., Venn, K. A., Lane, J. M. M., Lokhorst, D., & Yong, D. 2020, MNRAS, 497, 1236
Morinaga, Y., Ishiyama, T., Kirihara, T., & Kinjo, K. 2019, MNRAS, 487, 2718
Myeong, G. C., Evans, N. W., Belokurov, V., Amorisco, N. C., & Koposov, S. E. 2018a, MNRAS, 475, 1537
Myeong, G. C., Evans, N. W., Belokurov, V., Sanders, J. L., & Koposov, S. E. 2018b, ApJL, 856, L26
Myeong, G. C., Evans, N. W., Belokurov, V., Sanders, J. L., & Koposov, S. E. 2018c, ApJL, 863, L28
Myeong, G. C., Evans, N. W., Belokurov, V., Sanders, J. L., & Koposov, S. E. 2018d, MNRAS, 478, 5449
Myeong, G. C., Vasiliev, E., Iorio, G., Evans, N. W., & Belokurov, V. 2019, MNRAS, 488, 1235
Naidu, R. P., Conroy, C., Bonaca, A., et al. 2020, ApJ, 901, 48
Naidu, R. P., Conroy, C., Bonaca, A., et al. 2021, ApJ, 923, 92
Naidu, R. P., Ji, A. P., Conroy, C., et al. 2022, ApJL, 926, L36
Nataf, D. M., Gonzalez, O. A., Casagrande, L., et al. 2016, MNRAS, 456, 2692
Necib, L., Ostdiek, B., Lisanti, M., et al. 2020, ApJ, 903, 25
Neumayer, N., Seth, A., & Böker, T. 2020, A&ARv, 28, 4
Nidever, D. L., Holtzman, J. A., Allende Prieto, C., et al. 2015, AJ, 150, 173
Nidever, D. L., Hasselquist, S., Hayes, C. R., et al. 2020, ApJ, 895, 88

Nissen, P. E., & Schuster, W. J. 2010, A&A, 511, L10
Nomoto, K., Kobayashi, C., & Tominaga, N. 2013, ARA&A, 51, 457
Ochsenbein, F., Bauer, P., & Marcout, J. 2000, A&AS, 143, 23
Pallanca, C., Ferraro, F. R., Lanzoni, B., et al. 2021, ApJ, 917, 92
Pedregosa, F., Varoquaux, G., Gramfort, A., et al. 2012, arXiv:1201.0490
Perottoni, H. D., Amarante, J. A. S., Limberg, G., et al. 2021, ApJL, 913, L3
Pfeffer, J., Kruijssen, J. M. D., Crain, R. A., & Bastian, N. 2018, MNRAS, 475, 4309
Pfeffer, J., Lardo, C., Bastian, N., Saracino, S., & Kamann, S. 2021, MNRAS, 500, 2514
Piotto, G., Milone, A. P., Bedin, L. R., et al. 2015, AJ, 149, 91
Planck Collaboration, Aghanim, N., Akrami, Y., et al. 2020, A&A, 641, A6
Press, W. H., & Schechter, P. 1974, ApJ, 187, 425
Purcell, C. W., Bullock, J. S., & Kazantzidis, S. 2010, MNRAS, 404, 1711
Qu, Y., Di Matteo, P., Lehnert, M. D., & van Driel, W. 2011, A&A, 530, A10
Queiroz, A. B. A., Anders, F., Santiago, B. X., et al. 2018, MNRAS, 476, 2556
Queiroz, A. B. A., Anders, F., Chiappini, C., et al. 2020, A&A, 638, A76
Queiroz, A. B. A., Chiappini, C., Perez-Villegas, A., et al. 2021, A&A, 656, A156
Ramírez, I., Allende Prieto, C., & Lambert, D. L. 2013, ApJ, 764, 78
Rossa, J., van der Marel, R. P., Böker, T., et al. 2006, AJ, 132, 1074
Ruiz-Lara, T., Gallart, C., Monelli, M., et al. 2020, A&A, 639, L3
Sánchez-Janssen, R., Côté, P., Ferrarese, L., et al. 2019, ApJ, 878, 18
Santana, F. A., Beaton, R. L., Covey, K. R., et al. 2021, AJ, 162, 303
Santiago, B. X., Brauer, D. E., Anders, F., et al. 2016, A&A, 585, A42
Schönrich, R., Binney, J., & Dehnen, W. 2010, MNRAS, 403, 1829
Shank, D., Beers, T. C., Placco, V. M., et al. 2022, ApJ, 926, 26
Simion, I. T., Belokurov, V., & Koposov, S. E. 2019, MNRAS, 482, 921
Simpson, J. D., Martell, S. L., Da Costa, G., et al. 2020, MNRAS, 491, 3374
Souza, S. O., Kerber, L. O., Barbuy, B., et al. 2020, ApJ, 890, 38
Souza, S. O., Valentini, M., Barbuy, B., et al. 2021, A&A, 656, A78
Springel, V., Frenk, C. S., & White, S. D. M. 2006, Natur, 440, 1137
Tautvaišienė, G., Drazdauskas, A., Bragaglia, A., et al. 2022, A&A, 658, A80
Taylor, M. B. 2005, in ASP Conf. Ser. 347, Astronomical Data Analysis Software and Systems XIV, ed. P. Shopbell, M. Britton, & R. Ebert (San Francisco, CA: ASP), 29
Tinsley, B. M. 1979, ApJ, 229, 1046
Tissera, P. B., Scannapieco, C., Beers, T. C., & Carollo, D. 2013, MNRAS, 432, 3391
Tolstoy, E., Hill, V., & Tosi, M. 2009, ARA&A, 47, 371
Trick, W. H., Coronado, J., & Rix, H.-W. 2019, MNRAS, 484, 3291
van der Walt, S., Colbert, S. C., & Varoquaux, G. 2011, CSE, 13, 22
VandenBerg, D. A., Brogaard, K., Leaman, R., & Casagrande, L. 2013, ApJ, 775, 134
Vasiliev, E. 2019a, MNRAS, 484, 2832
Vasiliev, E. 2019b, MNRAS, 482, 1525
Vasiliev, E., & Baumgardt, H. 2021, MNRAS, 505, 5978
Veilleux, S., Cecil, G., & Bland-Hawthorn, J. 2005, ARA&A, 43, 769
Villalobos, Á., & Helmi, A. 2008, MNRAS, 391, 1806
Villalobos, Á., & Helmi, A. 2009, MNRAS, 399, 166
Villanova, S., Geisler, D., & Piotto, G. 2010, ApJL, 722, L18
Vincenzo, F., Spitoni, E., Calura, F., et al. 2019, MNRAS, 487, L47
Virtanen, P., Gommers, R., Oliphant, T. E., et al. 2020, NatMe, 17, 261
Wallerstein, G. 1962, ApJS, 6, 407
Wan, Z., Lewis, G. F., Li, T. S., et al. 2020, Natur, 583, 768
White, S. D. M., & Rees, M. J. 1978, MNRAS, 183, 341
Willman, B., & Strader, J. 2012, AJ, 144, 76
Yuan, Z., Myeong, G. C., Beers, T. C., et al. 2020, ApJ, 891, 39
Zolotov, A., Willman, B., Brooks, A. M., et al. 2009, ApJ, 702, 1058